On the accuracy of adiabaticity parameter estimations using magnetospheric models

John D. Haiducek[1], **Natalia Y. Ganushkina**[1,2], **Stepan Dubyagin**[2], **Daniel T. Welling**[1]

[1]Climate and Space Sciences, University of Michigan, Ann Arbor, MI, USA.

[2]Finnish Meteorological Institute, Helsinki, Finland

Key Points:

- Neither MHD nor empirical models can give reliable estimates of the adiabaticity parameter K.
- A method is proposed to correct model estimates of K using concurrent observations in the magnetotail.
- Corrected estimates of K are close to the $K = 8 - 10$ range expected for current sheet scattering.

This is the author manuscript accepted for publication and has undergone full peer review but has not been through the copyediting, typesetting, pagination and proofreading process, which may lead to differences between this version and the Version of Record. Please cite this article as doi: 10.1029/2018JA025916

Corresponding author: John D. Haiducek, jhaiduce@umich.edu

Abstract

Recent studies have found that even during quiet times, observed proton isotropic boundaries (IB) are often projected to the region of high adiabaticity parameter ($K \approx 30$), where $K = \frac{R_c}{r_g}$ is the ratio of magnetic field line radius of curvature to the particle gyroradius. This contradicts the accepted hypothesis that current sheet scattering (CSS) is the dominant mechanism of IB formation because $K \approx 8$ would be expected for this mechanism. We used magnetohydrodynamic (MHD) simulations and empirical models to compute K for 30 keV proton IB observations within three hours of local midnight. We found that neither class of model reliably estimates K unless supported by magnetic field observations in the current sheet. MHD simulations produced higher K values than expected for CSS ($K = 15 - 30$), and empirical models gave lower values ($K < 4$).

We obtained reliable estimates of K by controlling for the accuracy of the normal component and the gradient of the radial component in the neutral sheet, using observations from three THEMIS satellites. For the first time, we demonstrated that both these variables should be taken into account for the accurate estimation of the curvature radius. This greatly reduced the spread of K values, indicating that much of the previous spread was due to errors in the magnetic field, but also that these errors can be controlled. Most of the corrected values fall within the expected range for CSS, supporting the hypothesis that the IB's were formed by CSS. Accounting for all model results, we obtain an average corrected value of $K = 6.0$.

1 Introduction

Determining the structure of the Earth's magnetic field under various solar wind conditions is essential for understanding the relationship between ionospheric features and magnetospheric processes. This requires having magnetic field vectors throughout the relevant parts of the magnetosphere, so that field lines can be traced between the ionosphere and the magnetotail. At present, the available spacecraft observations are sparsely distributed, and magnetospheric models play a crucial role by providing estimations of the magnetic field throughout the geospace environment.

One way to gain insight into field line mappings is by studying the isotropic boundary (IB), a distinct feature that can be used to probe connections between the ionosphere and magnetosphere. The IB refers to a latitude in the auroral zone at which a substan-

tial change occurs in the flux of downwelling particles into the ionosphere. Equatorward of the IB, the flux in directions perpendicular to the local magnetic field well exceeds the downwelling flux parallel to the local magnetic field. Poleward of the IB, comparable fluxes are detected in the directions parallel and perpendicular to the field. This has been observed by many satellites, including Injun 1 and 3, ESRO IA and IB, NOAA, and DMSP [*Søraas*, 1972; *Imhof et al.*, 1977; *Sergeev et al.*, 1983; *Newell et al.*, 1998]. For protons, the IB is observed in all MLT sectors and at all activity levels [*Sergeev et al.*, 1993].

The difference in loss-cone filling poleward and equatorward of the IB indicates that the particles observed at the IB originate from a transitional region within the magnetosphere, in which the rate of pitch angle scattering changes significantly. On the night side, one mechanism for this is a transition from adiabatic to chaotic particle motion as particles cross the current sheet, a process termed current sheet scattering (CSS) [*West et al.*, 1978; *Büchner and Zelenyi*, 1987; *Sergeev et al.*, 1993]. This occurs when the radius of curvature of the local magnetic field line, R_c, becomes comparable to the effective particle gyroradius r_g [*Alfvén and Fälthammar*, 1963; *Tsyganenko*, 1982; *Büchner and Zelenyi*, 1987; *Delcourt et al.*, 1996], and the strength of this scattering process is parameterized by the ratio $K = R_c/r_g$. That the CSS mechanism results in isotropic precipitation from the plasma sheet is undisputed, because for $K < 1$ the particle motion in the plasma sheet is chaotic [see e.g. *Coroniti*, 1980; *Lyons and Speiser*, 1982; *Chen and Palmadesso*, 1986; *Büchner and Zelenyi*, 1987; *Sergeev and Gvozdevsky*, 1995]. In general the IB may be formed by other processes, most importantly the interaction of particles with electromagnetic ion-cyclotron (EMIC) waves [*Kennel and Petschek*, 1966; *Liang et al.*, 2014; *Sergeev et al.*, 2015a,b]. The role of such interactions in particle precipitation has long been recognized [see e.g. the review paper by *Hultqvist*, 1979]. However, EMIC waves cannot always be responsible for IB formation, because the intensity of EMIC waves varies strongly with activity and MLT [e.g. *Bräysy et al.*, 1998; *Halford et al.*, 2010; *Usanova et al.*, 2012]. A number of efforts have identified pitch-angle scattering due to CSS as the main source for particle precipitation from the magnetotail during quiet conditions [*Sergeev and Tsyganenko*, 1982; *Sergeev et al.*, 1993; *Ganushkina et al.*, 2005]. CSS does not require the presence of waves and can explain the fact that the IB is observed in all activity levels and all MLTs on the night side. However, scattering by waves can sometimes cause the IB to form at a different latitude than would occur for CSS, particularly during storms and sub-

storms [*Søraas et al.*, 1980; *Gvozdevsky et al.*, 1997; *Yahnin and Yahnina*, 2007; *Sergeev et al.*, 2010; *Dubyagin et al.*, 2018], and there is evidence for IB formation by waves during quiet periods as well [*Sergeev et al.*, 2015b].

When the CSS mechanism is responsible for IB formation, the IB location is determined by the field geometry. This enables the IB latitude to be used to estimate the degree of magnetotail field stretching [*Sergeev et al.*, 1993; *Sergeev and Gvozdevsky*, 1995; *Meurant et al.*, 2007]. This motivates further study of the role of CSS in IB formation, in order to better determine the conditions under which CSS (as opposed to scattering by EMIC waves or some other process) is the controlling mechanism responsible for IB formation. One means to do so is by estimating the value of K associated with observed IB locations. Numerical tracing of particle trajectories from the current sheet [e.g. *Delcourt et al.*, 1996, 2000, 2006] has shown that CSS acts when $K \lesssim 1 - 10$ (a range spanning an order of magnitude). *Delcourt et al.* [1996] noted significant dependence on the incident particle population. However, in analysis it is often useful to use a specific critical value (rather than a range) as the threshold for CSS, and for this purpose many researchers have used $K_{crit} = 8$ as originally proposed by *Sergeev et al.* [1983].

To determine whether the IB is associated with CSS requires mapping IB observations to the current sheet, and estimating K there. Both steps require a magnetic field model of some kind. A number of previous efforts, including *Sergeev et al.* [1993], *Ganushkina et al.* [2005], *Sergeev et al.* [2015b], and *Dubyagin et al.* [2018], have accomplished this using empirical models such as the Tsyganenko models. Such models have good traceability to observational data since they are constructed by fitting to available satellite measurements. However, such models tend to be limited to representing features that are resolved by the observational data used in their construction or represented in the form of the equations that are fit to that data. Global first-principles models such as magnetohydrodynamic (MHD) and hybrid simulation codes offer an alternative. Such models have the potential to produce features that are governed by the physics incorporated in the models, without necessarily requiring observational data that resolves those features directly. This makes first-principles models potentially useful in understanding the IB, which depends on the magnetic configuration in the magnetotail, a region that is highly dynamic and only sparsely covered by observational data.

To date, only *Gilson et al.* [2012] and *Ilie et al.* [2015] have used MHD models to explore the IB and its properties. Of these, *Ilie et al.* [2015] is of particular interest to us because they mapped the locations of in situ IB observations through the MHD fields to estimate K in much the same way as was previously done with empirical models. That effort focused on a one-day quiet interval on February 13, 2009, using IB observations obtained from the Medium Energy Proton and Electron Detector (MEPED) instruments [*Evans and Greer*, 2000] on the NOAA/POES and METOP spacecraft. A quiet interval was chosen in order to reduce the chance of particle scattering due to wave-particle interactions. Nonetheless, the estimates of K derived from MHD ranged from 27 to 44, unexpectedly high values for K associated with quiet-time IB.

Many of the above studies produced K values covering a fairly wide range. Moreover, since most use only a single model to map the IB to the magnetotail and to compute K, it is generally not possible to tell what part of this wide variation is due to differences in the actual state of the magnetosphere (either in the field geometry or the action of other scattering mechanisms such as waves) and what part is due to differences between models and observational methodologies. Using multiple models to study the same event in combination with in situ magnetic field observations will provide a means to distinguish variation in K due to model error from variation due to physical causes.

The goals of this paper are twofold: 1) Determine whether MHD is capable of estimating K correctly for quiet-time IB observations 2) Provide better constraints on the range of K values associated with night-side IB formation during quiet time. The paper is organized as follows: Section 2 describes the event and the observations used to identify the IB locations from the observations. Section 3 gives the methodology used, including details of the three MHD simulations used in this paper, and the procedures used for field tracing and for computing K. Section 4 presents comparisons of the MHD simulations to magnetic field observations. Section 5 gives the results of the field line tracing from the IB locations using MHD, and gives the computed K values for all the IB crossings. Section 6 presents results of field line tracing and resulting K values obtained using the empirical models. Section 7 compares the two classes of models and shows results of the K correction procedures. Section 8 discusses the implications of these results in the context of previous studies.

Figure 1. Solar wind observations and geomagnetic indices from 13 February, 2009. a) flow speed, b) proton density, c) temperature, d) B_z (GSM), e) Sym-H, f) Kp, g) AL

2 Event and observations

We analyze the IB observations and their associated K values for the 24 hour interval beginning at midnight UTC on 13 February, 2009. This interval was selected because it is a quiet period in terms of solar wind driving and geomagnetic activity (AL>-150 nT, Sym-H>-10, Kp<2), and because of the availability of magnetic field observations in the night-side magnetosphere from the five THEMIS spacecraft. THEMIS A, D, and E had apogee at distances of 11.6-11.7 R_E, near the region that is expected to map to the IB, while THEMIS B and C had apogee at distances of 28.6 and 19.4 R_E, respectively.

Figure 1 shows the solar wind driving conditions on this day, as well as the geomagnetic indices Sym-H, Kp, and AL. The solar wind velocity (Figure 1a) ranged from 298 to 335 km/s with no noticeable discontinuities, the proton density (Figure 1b) ranged from 2.9 to 12 cm^{-3}, and the B_z component of the IMF (Figure 1c) remained within ±3 nT. The solar wind temperature (Figure 1d) ranged from 1.1×10^5 to 7.2×10^5 K. The minumum Sym-H (Figure 1e) was -6 nT, the maximum Kp (Figure 1f) was 1.3, and the minimum AL (Figure 1g) was -128 nT. Two negative diversions appear in the AL index near the end of the day, but neither is strong enough to be considered a substorm. For instance, neither the list from *Borovsky and Yakymenko* [2017] obtained using SML, nor the list from the SuperMag website (http://supermag.jhuapl.edu/substorms/) produced using the *Newell and Gjerloev* [2011] algorithm contain any substorms during this period.

Isotropic boundaries were identified using proton flux data from the MEPED instruments on board several NOAA/POES and METOP spacecraft. The MEPED instrument, which is described in *Evans and Greer* [2000], includes two telescopes, which measure proton fluxes in four energy bands ranging from 30 to 6900 keV. The first telescope, called the 0° telescope, is within 10° of the spacecraft's zenith direction (i.e. away from Earth). At high latitudes this direction places the 0° telescope close to the direction of the local magnetic field, so that it primarily detects precipitating particles. The second telescope, termed the 90° telescope, is oriented nearly orthogonal to the 0° telescope. The 90° telescope primarily detects locally trapped particles.

The IB locations used in this paper are the same as those from *Ilie et al.* [2015]. These were determined from the MEPED P1 energy channel (30-80 keV). Although the nominal low energy limit of the P1 channel is 30 keV, it is actually somewhat higher and varies among the satellites due to detector degradation. In addition, the 90°- telescopes degrades more strongly than 0°-telescope. Table 1 shows the low energy limits for 0°- telescope as given by *Asikainen et al.* [2012]. To recalibrate 90°- telescope data to the 0°- telescope energy limit, we use procedure described in the Appendix of *Dubyagin et al.* [2018]. After this correction, we found IB crossings using the procedure in *Dubyagin et al.* [2013] which identifies a poleward and equatorward limit for the IB location. Identifying a poleward and equatorward limit for the IB gives an uncertainty range of latitudes for each IB crossing, which was less than 0.3° for the selected events [*Ilie et al.*, 2015]. The criteria for determining the equatorward limit of the IB were chosen to avoid identifying brief periods of isotropic or nearly isotropic fluxes near the low-latitude limit of the auroral oval, which may be the result of wave-particle interactions [*Gvozdevsky et al.*, 1997; *Yahnin and Yahnina*, 2007]. In total, 94 IB crossings were identified from five ionospheric satellites (NOAA 15-18 and METOP-02) using this procedure, of which 27 were within three hours MLT of local midnight. As an additional measure to reduce the chances that the selected IB observations could be influenced by wave-particle interactions, only those IB observations that were of typical appearance were used. Typical appearance means a sharp transition from an empty loss cone on the low-latitude side of the IB to a filled loss cone on the high-latitude side, with both the 0° and 90° fluxes reaching a maximum on the high-latitude side of the IB, followed by a monotonic decrease in fluxes going toward the polar cap. Rather than using all suitable IB observations, we include only those for which the THEMIS A, D, or E spacecraft was within ±1 hour MLT of the location of the IB observation, and within the radial distance range of $r = 7 - 10$ R_E from the Earth. For the purpose of this paper we consider spacecraft satisfying these criteria as being conjugate with the IB location. We use observations from these conjugate spacecraft to test the accuracy of the model magnetic fields in the magnetotail, and to correct for errors in those fields. After eliminating the IB observations that were of atypical appearance and those without suitable THEMIS observations, the final list consisted of 7 IB observations, which are shown in Table 1.

An illustration of the locations of the THEMIS A, D, and E spacecraft is shown in Figure 2. Figure 2a shows the positions of THEMIS A (represented by blue squares) in

Satellite	Time	Detector energy (keV)	Mag. Lat.	MLT
METOP-02	2009-02-13/01:41:16	36	-68.06	22.77
METOP-02	2009-02-13/03:22:00	36	-67.97	0.04
NOAA-16	2009-02-13/02:23:16	45	-67.98	23.97
NOAA-16	2009-02-13/02:25:23	45	-68.11	22.82
NOAA-17	2009-02-13/02:41:34	45	-68.01	23.50
NOAA-17	2009-02-13/04:22:02	45	-68.34	0.91
NOAA-18	2009-02-13/16:54:17	30	67.83	2.53

Table 1. Times and locations of the IB observations, as well as detector cutoff energies for each spacecraft.

Figure 2. (a) THEMIS A location for the times of the IB observations. (b) and (c) Relative locations of THEMIS A, D, and E at 4:22 UT.

the GSM $z = 0$ plane at the time of selected IB observations. The spacecraft was located near midnight for six of the seven IB observations. For the seventh, it was located closer to dawn, though still more than 5 R_E down-tail. Figures 2b and 2c show the relative locations of THEMIS A, D, and E at 4:22 UT. THEMIS D is represented by a purple upward-pointing triangle, while THEMIS E is represented by a red downward-pointing triangle. It is apparent that THEMIS A and E are separated significantly in the z direction (more than 1 R_E apart), but are more closely spaced in the x and y directions. This enables us to estimate gradients in the z direction by comparing values at THEMIS A and E, which we will use in Section 7 to estimate the influence of errors in R_c on the K values computed by the models.

3 Methodology

Having obtained the list of IB observations in Table 1 which are conjugate with the THEMIS A, D, or E spacecraft, we next proceed to computing K at a magnetotail location corresponding with each IB observation. This will provide an indication of whether the estimated field geometry is consistent with CSS for the observed IB crossings. Neither the mapping nor the computation of K can be accomplished directly from the available observational data due to the small number of satellites operating in the magnetotail. Therefore

we require models to estimate the magnetic fields in order to do both the mapping and the K calculation. We begin by tracing a field line from each IB observation using the model-derived magnetic fields. Along this field line we find the location were $|B|$ reaches its minimum, and there compute $K = R_c/r_g$ from the model-derived magnetic fields. The tracing and the K calculation are accomplished using magnetic fields obtained from several models, including three MHD simulations performed using the Space Weather Modeling Framework (SWMF) [*Tóth et al.*, 2005] and six empirical Tsyganenko models: *Tsyganenko* [1995] (T96), *Tsyganenko* [2002] (T01), *Tsyganenko and Sitnov* [2005] (TS05), *Tsyganenko and Andreeva* [2015] (TA15N and TA15B), and *Tsyganenko and Andreeva* [2016] (TA16RBF). The SWMF simulations are described in detail later in this section, and the Tsyganenko models are described in Section 6.

For each field line traced, we search for the point where $|B|$ reaches its minimum. At the location of $|B|_{min}$, the field line radius of curvature is computed as

$$R_c = \frac{1}{|(\mathbf{b} \cdot \nabla)\mathbf{b}|}, \tag{1}$$

where $\mathbf{b}$ is the unit vector along the magnetic field direction, and $\nabla\mathbf{b}$ is computed using a two-point centered difference. We then compute the effective particle gyroradius r_g. When computing r_g, we take the low energy limit of the detector as the particle energy. As mentioned earlier, the detector energy limit varies among the different satellites due to the degradation of the detectors over time [*Asikainen et al.*, 2012], and the values used for each spacecraft are shown in Table 1.

Our SWMF simulations consist of the Block Adaptive Tree Solar-Wind, Roe-Type Upwind Scheme (BATS-R-US) MHD model [*Powell et al.*, 1999; *DeZeeuw et al.*, 2000], coupled with the Rice Convection Model (RCM) [*Wolf et al.*, 1982; *Sazykin*, 2000; *Toffoletto et al.*, 2003] and the Ridley Ionosphere Model (RIM) [*Ridley and Liemohn*, 2002; *Ridley et al.*, 2004]. The inputs to the model were solar wind parameters obtained from the 1-minute OMNI dataset provided by the NASA Goddard Spaceflight Center (GSFC), and the F10.7 radio flux observed at Penticton, BC [*Tapping*, 2013].

We ran three SWMF simulations, with the same inputs but with differences in grid resolution, numerical scheme, and coupling parameters. By testing different settings of SWMF we are able to determine in a general sense how sensitive the results are to various

SWMF settings. The first SWMF simulation, henceforth referred to as "SWMFa," used settings based on those in *Ilie et al.* [2015]. The settings of SWMF differ from those used in *Ilie et al.* [2015] in the following ways:

- The simulation in *Ilie et al.* [2015] paper used a dipole moment of 31.1 μT oriented at 289.1° geographic longitude and 79.0° latitude, which was the default in SWMF at the time. The simulations for the present paper used the IGRF dipole parameters for February 13, 2009, which were 287.86° geographic longitude and 79.96° latitude, and a dipole moment of 29.97 μT.
- Minimum values for pressure and density were set to improve numerical stability
- The numerical scheme was changed from an implicit-explicit scheme to a fully explicit one in order to improve stability. The switch to fully explicit in turn required a reduction in the time step.

The grid of SWMFa is the same as was used in *Ilie et al.* [2015], and contains about 4 million cells. The minimum cell size is 1/8 R_E near the Earth, and the maximum cell size is 2 R_E at the outflow boundaries.

The other two SWMF simulations used settings previously described in *Haiducek et al.* [2017]. The first of these, termed "Hi-res" in *Haiducek et al.* [2017], is identified as "SWMFb" in this paper. SWMFb used a grid with about 2 million cells. The grid for SWMFb was the same as that used in SWMFa within the near-Earth region (out to about 60 R_E in each direction). Beyond 60 R_E, SWMFa used a 2 R_E resolution everywhere. SWMFb, on the other hand, used a 1 R_E cell size in the current sheet region out to 120 R_E, and beyond 120 R_E the cell size increases until reaching 8 R_E near the outflow boundaries. As a result, SWMFb had a higher resolution in the current sheet region but a smaller total number of cells due to coarser resolution in the deep tail (120 R_E and beyond). Besides the grid refinement, SWMFb differed from SWMFa in terms of the RCM settings. In the coupling between BATS-R-US and RCM, SWMFb used the *Young et al.* [1982] composition model to determine the ratio of oxygen to hydrogen in the coupling with RCM, where SWMFa used a fixed ratio. Finally, an ad hoc decay was applied to the RCM ring current in SWMFb, which is designed to improve agreement with observations during storm recovery but is not expected to affect the quiet-time results substantially.

The final simulation, termed "SWMFc," was also described in detail in *Haiducek et al.* [2017], and in that paper was referred to as the "SWPC" simulation due to the settings being largely the same as those used operationally at NOAA Space Weather Prediction Center (SWPC). SWMFc used a coarser grid than either SWMFa or SWMFb, with a minimum cell size of 1/4 R_E near the Earth, a maximum cell size of 8 R_E at the outflow boundaries, and no additional refinement in the tail or current sheet. The RCM coupling settings were the same as SWMFb except that a fixed oxygen to hydrogen ratio was used.

For all of the SWMF simulations, field lines were traced through the MHD domain from the location of each IB crossing identified using the MEPED data. This was done once every minute of simulation time. The inner boundary of the MHD domain lies at 2.5 R_E from the center of the Earth (rather than at the surface). Since the altitudes of the NOAA and METOP spacecraft were lower than this, the IB locations were mapped to 2.5 R_E prior to tracing through the MHD domain. In order to minimize the influence of non-dipole harmonics on the mapping, we implemented the mapping by first transforming the IB locations into altitude adjusted corrected geomagnetic coordinates [AACGM, *Baker and Wing*, 1989], with the reference height set to 0 km. After conversion to AACGM coordinates, each IB location was mapped to 2.5 R_E using a dipole field. Within the MHD domain, the field lines were traced using a third order Runge-Kutta scheme with a second-order error estimator and adaptive step size.

4 Validation of magnetic fields with magnetospheric satellite observations

In order to verify the accuracy of the SWMF in estimating the magnetic field geometry, we compared the magnetic fields estimated by SWMF along the orbits of the GOES and THEMIS satellites with observations from the fluxgate magnetometers onboard the spacecraft [*Singer et al.*, 1996; *Auster et al.*, 2008] during the time from 0000 to 1800 UT on February 13, 2009. This time period includes all of the IB observation times listed in Table 1. For the THEMIS spacecraft, we additionally restrict the analysis to points in time for which the spacecraft was at least 7 R_E from the Earth, since this was the minimum distance used for including a THEMIS spacecraft in analysis of an IB event. As an example, Figure 3 shows fields at THEMIS A. Plots for THEMIS B-E and GOES 11 and 12 are included in the supplemental data. In Figure 3, time series plots of the magnetic fields estimated by each SWMF simulation are overlaid on top of a plot of the observed magnetic field. The observational data is shown in light blue, SWMFa in medium blue,

SWMFb in orange, and SWMFc in green. The left hand column (Figures 3a, 3c, and 3e) shows the B_x, B_y and B_z (GSM) components of the total magnetic field. The right hand column (Figures 3b, 3d, and 3f) shows the same components for the external magnetic field. We obtain the external field by subtracting a dipole field from the total field, with the parameters of the dipole being the IGRF parameters given in Section 3 that were used within the SWMF simulations. The same dipole field was subtracted from both from the model and from the observed total fields to obtain the respective external fields. Throughout Figure 3, the times of the IB observations listed in Table 1 are denoted with vertical dotted lines. Note that the IB observations at 02:23 and 02:25 UT were very close together in time, and while individual lines are drawn for those two events, they are difficult to distinguish in the plot.

Figure 3. Magnetic field components in GSM coordinates at the THEMIS A satellite, observed and predicted, for February 13, 2009. Left column shows the total field, while the right column shows the external field (intrinsic field of the Earth removed). Spacecraft locations in MLT and GSM coordinates are displayed below the time scale.

The B_x component of the total field (Figure 3a) is consistently negative throughout the time period shown. This indicates that the spacecraft was located south of the current sheet. The largest discrepancy between the modeled and observed B_x is an overestimation of the magnitude of B_x by SWMFb and SWMFc between 0800 and 1600, visible in both Figures 3a and 3b, with the greatest overestimation being 12.0 nT by SWMFb at 10:44 UT. Since the difference is present in the external field, it must be due to differences in magnetospheric currents. The underestimation of the magnitude of B_x indicates that the the current sheet in the simulation was farther north than actual, or that the model current sheet was thinner or contained stronger currents than the actual one, resulting in a stronger gradient in B_x across the current sheet. The data in Figure 3a cannot distinguish between these two explanations, but given the finite grid resolution of the model it is more likely that the current sheet would be thicker than observed rather than thinner, in which case the underestimation of the B_x magnitude indicates an error in the current sheet location.

The estimation of the B_y component (Figure 3d) is somewhat more accurate than that of B_x. All three models miss two negative diversions of the observed B_y that occur at 0800 and 1230 UT. The largest discrepancy is an underestimation (in magnitude) of 7.6

nT by SWMFc at 17:45 UT, at which time the external B_y in SWMFc is -2.1 nT while the observations and the estimations by SWMFa and SWMFb are all around -10 nT. At 17:45 UT the spacecraft was moving toward the Earth, and the B_y component of the total field was around -50 nT (Figure 3c).

From the external B_z plot (Figure 3f) it is apparent that all three model configurations tend to overestimate B_z throughout the time period of the plot, though there are a few brief periods of underestimation by SWMFa and SWMFb. The largest discrepancy is an overestimation of 11.2 nT by SWMFc at 0131 UT. This occurs at a time when the B_z component of the total field was around 70 nT (Figure 3e). An overestimation of B_z was previously reported for SWMF in *Ganushkina et al.* [2010].

Similar results were obtained for THEMIS D and E as for THEMIS A. For THEMIS B and C the behavior of the observed magnetic field was substantially different from THEMIS A, D, and E due to the THEMIS B and C spacecraft having apogee farther down-tail. The model delivered similarly close estimations for the GOES 11 and 12 magnetic fields: The greatest diversion from observations by any single component was 13.3 nT, and most SWMF estimations were within 5 nT of observations. A persistent overestimation of B_z (like that seen at THEMIS A) was found at GOES 12 but not at GOES 11.

The SWMF simulations estimated the fields with reasonably good accuracy overall. Many differences are present in the behavior of transient features, but typically the differences between the model and observations even during these transients are of a magnitude of only a few nT, and the differences only occasionally exceed 10 nT. The general behavior of the fields is captured well by the simulation, and we find the estimations to be of sufficient quality to warrant their use in studying the IB.

5 Mapping locations of isotropic boundaries with MHD

Having verified that the SWMF simulations give reasonably good estimations of the magnetic fields in the magnetotail, we proceed to tracing magnetic fields from the locations of the IB observations. This will enable us to use the SWMF output to obtain information about the conditions leading to IB formation. Figure 4 shows the results of tracing field lines from two of the IB observations through the magnetic fields computed by the SWMFb MHD simulation. These two events were selected as representative examples from the total of 21 traces (7 IB observations and 3 model runs). The left column (panels

a-e) show the IB crosssing at 0225 UT, while the right column (panels f-j) shows the IB crossing at 0422 UT. Panels a and f show the location of the IB observation, the field line traced from the IB location, and satellite locations in the GSM x-y plane. Panels b and g show the same in the x-z plane. The Earth is denoted by a black circle, and surrounded by a grey circle representing the inner boundary of the MHD domain. The location of the observed IB, mapped to the inner boundary of the MHD domain, is denoted with a small circle. The locations of the THEMIS A and E spacecraft are also shown. The field line traced from the IB location is shown as a dashed line, and the minimum $|B|$ point along this field line is denoted by an "X."

Figure 4. Example of tracing field lines for two IB crossings, using the MHD solution from the SWMFb simulation. Left column: IB crossing of the NOAA-16 spacecraft at 02:25 UT; right column: IB crossing of the NOAA-17 spacecraft at 04:22 UT. (a), (b), (f), and (g) show the IB location, field line traced from the IB location, and satellite positions in the GSM x-y and y-z planes. The IB location (mapped to 2.5 Re) is shown as a small circle. A dashed line denotes the field line traced from this location, projected into the plane of the figure. The minimum B point along this line is denoted with an "X." Locations of THEMIS A and E spacecraft are shown using the same symbols as in Figure 2. A solid line denotes a radial line through the minimum B point, projected into the minimum B surface and subsequently into the the plane of the figure. This line crosses the field line at the X. The remaining plots show quantities computed along this line, as a function of GSM x. (c) and (h) show $|B|$, (d) and (i) show magnetic field line radius of curvature R_c, and (e) and (j) show K.

By tracing the field lines within each SWMF simulation, we computed a surface defined by $|B| = |B|_{min}$ along each field line. The solid line extending outward from the Earth in Figures 4a, 4b, 4f, and 4g denotes a radial line in this surface from the center of the Earth through the point where the IB field line intersects the minimum $|B|$ surface. Figures 4c-4e and 4h-4j show simulation output along this minimum $|B|$ line as a function of x in GSM coordinates. The location where the IB field line intersects this surface is denoted with an "X."

Figures 4c and 4h show $|B|$ along the minimum $|B|$ line described above. Figures 4d and 4i show R_c, the field line radius of curvature, along the minimum $|B|$ line. In both cases, the point that maps to the IB location (denoted with an "X") occurs near the maxi-

mum of R_c. This local maximum indicates a transition from a dipolar to a stretched field configuration. Within a dipolar field, the radius of curvature increases linearly with distance, so the presence of a local maximum indicates that the field has diverged significantly from dipolar. At the same time, $|B|$ is continuing to decrease rapidly, resulting in an increase in the gyroradius r_g and making it increasingly likely that the conditions for adiabatic motion will be violated. Similar plots of R_c as a function of x can be found in *Sergeev and Tsyganenko* [1982] and *Yue et al.* [2014], in both cases produced using empirical magnetic field models, and these exhibit generally similar behavior. The R_c plots in both *Sergeev and Tsyganenko* [1982] and *Yue et al.* [2014] reaches a maximum at a somewhat closer distance to the Earth and drops off more rapidly compared to the plots in Figures 4c and 4h of the present paper. However, the behavior of R_c in the magnetotail is quite volatile and depends strongly on local conditions in the plasma sheet and on the general disturbance level of the magnetosphere.

The plots in Figures 4c and 4h show larger R_c than either *Sergeev and Tsyganenko* [1982] or *Yue et al.* [2014]. The position at which the maximum R_c occurs is also slightly farther from the Earth than in *Yue et al.* [2014]. This indicates that the MHD fields shown in this figure are less stretched than those shown in the similar figures of *Sergeev and Tsyganenko* [1982] and *Yue et al.* [2014].

A local maximum of R_c combined with a rapidly falling $|B|$ implies a move toward conditions favorable for pitch angle scattering. However, the point where pitch angle scattering occurs is controlled more directly by K. Figures 4e and 4j show K as a function of x. K is shown on a logarithmic scale; the motivation for the logarithmic scsale will be addressed later. For both of these, K decreases monotonically as a function of x. The K values at the points mapped from the IB locations (the points marked with an "X") in Figure 4e and 4j are 18.9 and 26.0, respectively.

From Figures 3 and 4 we see that the SWMF simulations are tending to produce magnetic fields that are more dipolar (less stretched) than actual, resulting in larger B_z, and likely causing an overestimate of K. We can quantify the discrepancy in the field stretching by directly comparing with available in situ magnetic field measurements for each IB observation. For this purpose, we use in situ B observations from the THEMIS satellites that are conjugate with each IB observation under the criteria specified in Section 2. We define $\overline{\Delta B_z} = \overline{(B_{z_{model}} - B_{z_{observations}})}$ as the average of error in B_z at the

Figure 5. K as a function of the error $\overline{\Delta B_z}$ averaged over the THEMIS spacecraft that were conjugate with each IB. Black line denotes a fit to the SWMFa and SWMFc points.

spacecraft that are conjugate with each IB observation. Figure 5 shows K as a function of $\overline{\Delta B_z}$ for all simulations and all the IB observations shown in Table 1. The y-axis of Figure 5 is shown on a logarithmic scale. It is apparent from the figure that the K values obtained from SWMFa and SWMFc show a common dependence on $\overline{\Delta B_z}$. A least squares fit to the combined K estimates from SWMFa and SWMFc is plotted on top of the points. K estimates from SWMFb have been omitted from the fit because they exhibited a substantially different dependence on K: Fitting to the SWMFb points produces a lower slope and higher intercept, while the SWMFa and SWMFc data had similar slopes and intercepts to each other. To assess the quality of the fits, we use coefficient of determination (R^2), defined as

$$R^2 = 1 - \frac{\sum_i (K_i - \overline{K})^2}{\sum_i (K_i - f(\overline{\Delta B_z}))^2}, \tag{2}$$

where $f(\overline{\Delta B_z})$ is the regression curve. R^2 represents the fraction of the variation in K that is explained by $f(\overline{\Delta B_z})$, and for a perfect fit we would get $R^2 = 1$. For SWMFb, R^2 was only 0.02, while SWMFa and SWMFc had R^2 values of 0.65 and 0.60, respectively. The poor fit for SWMFb seems to be due in part to the influence of outlier points and in part to the points being clustered in a fairly narrow range of $\overline{\Delta B_z}$.

The common dependence of K on $\overline{\Delta B_z}$, and the fact that it is similar for both SWMFa and SWMFc, can be explained by first noting that K can be approximated by

$$K = \frac{R_c}{r_g} \approx \frac{qB_z^2}{\sqrt{2mE}\, dB_r/dz}, \tag{3}$$

where q denotes the particle charge, m the particle mass, and E the particle energy. B_r is the radial component of magnetic field in GSM coordinates, defined as

$$B_r = \frac{xB_x + yB_y}{\sqrt{x^2 + y^2}}. \tag{4}$$

Since we are working with protons, q and m are the elementary charge and the proton mass. B_z and B_r denote the magnetic field z and radial components in GSM coordinates. This expression indicates a quadratic relationship between B_z and K. We take the logarithm of both sides to obtain $\log K \propto \log B_z$, and then linearize the right hand side of the equation to obtain

$$\log K = A_1 + A_2\overline{\Delta B_z}, \tag{5}$$

which is the expression for the fit curve shown in Figure 5. A_2 represents the linear dependence of K on B_z, which is the result of both the expression for K and the characteristics of the model and the physical system it represents. By setting $\overline{\Delta B_z} = 0$ we obtain $K_0 = \exp(A_1) = 16$, an estimate of the average K in the absence of B_z error. In order to determine the uncertainty associated with A_1, we estimate the 95% confidence interval for the intercept A_1 as described in e.g. *Montgomery et al.* [2012]. The 95% confidence interval for $\exp(A_1)$ is [13, 19], indicating that the intercept value of $K_0 = 16$ is significantly lower than the value of $K = 33$ reported in *Ilie et al.* [2015], but also significantly higher than the commonly used threshold value $K_{crit} = 8$ [*Sergeev et al.*, 1983].

6 Estimation of K using empirical models

In this study we use the following empirical magnetospheric models: *Tsyganenko* [1995] (T96), *Tsyganenko* [2002] (T01), *Tsyganenko and Sitnov* [2005] (TS05), *Tsyganenko and Andreeva* [2015] (TA15N and TA15B), and *Tsyganenko and Andreeva* [2016] (TA16RBF). For all these models, the magnetic field is built as a sum of analytical functions of the model's driving parameters. These functions can represent separate current systems (T96–TA15), or just be basis functions which have no counterpart among conventional current systems in the magnetosphere. Below we briefly summarize the model's features which can be critical for K-parameter estimation. Since we analyze a quiet event, the ring current is very weak and the magnetic field at the region of expected IB formation as well as ionosphere-magnetosphere mapping are mostly controlled by the tail current system.

The distinctive feature of the T96 model is its optimization for an accurate ionosphere magnetosphere mapping: the angular difference between the modeled and observed magnetic field vectors was minimized when T96 was fitted to observed magnetic field vec-

tors. For all other models, the squared difference of magnetic field components was minimized. On the other hand, since T96 is the earliest model, its structure is rather simple. The T96 tail current thickness and position with respect to the Earth is fixed and only its intensity changes with activity which is parameterized by Akasofu epsilon parameter.

The T01 model represents a further development of the concept used for T96. The T01 tail model thickness does not vary with activity but the tail current inner edge moves towards the Earth when activity grows. In addition, the tail module includes two independent sub-modules which add a flexibility to the tail current radial profile.

The TS05 model was specially designed to describe the magnetosphere during storm-time disturbances. The model was fit to the measurements made during storm intervals and likely should not be used for modeling a quiet event. Its tail current thickness and position vary with activity which is parameterized by complex integral functions of the solar wind plasma and IMF parameters taking into account the prehistory of the conditions in the solar wind. TS05 has the most advanced parameterization of geomagnetic activity among all empirical models.

The TA15 model is a forecasting model which is parameterized entirely by external parameters (no ground-based indices are used). The tail current thickness and position vary with activity and the current intensity is assumed to fall off with distance as a power law. There are two versions of the model referred to as TA15N, parameterized by the universal coupling function described in *Newell et al.* [2007], and TA15B, parameterized by an external driving function described in *Boynton et al.* [2011].

It should be noted, that for T96–TA15 models, to a large extent, the current system geometries are determined in an ad hoc manner. For example: although the tail current thickness in TS05 and TA15 models can vary with activity, its variance with activity is parameterized for the current sheet as a whole, and its variance with X and Y is defined by a realistic but arbitrary function. This drawback was corrected in the TA16RBF model where the field is represented as a sum of elementary functions, each depending on activity parameters including the universal coupling function of *Newell et al.* [2007]. This approach minimizes the role of the authors in the current geometry definition. However, the amount of the existing spacecraft measurements does not allow the model to resolve fine spatial structures.

Figure 6. Results of K estimation for the four empirical models. Black line denotes a least-squares fit to all points except those produced by TS05.

Using these models and geomagnetic dipole to represent the Earth's inner field, we traced the field lines from IB locations (in AACGM coordinates). The standard field line tracing subroutine from Geopack FORTRAN package was used. The package as well as the model input driving parameters can be found at http://geo.phys.spbu.ru/~tsyganenko/modeling.html. $K = \frac{R_c}{r_g}$ was estimated at the minimum magnetic field point (in the equatorial part of the field line), using Equation 1 to estimate R_c and the cutoff energies from Table 1 to estimate r_g. The output from the models was also computed at the locations of the THEMIS probes and was compared with THEMIS observations.

Figure 6 shows the computed K values versus $\overline{\Delta B_Z}$ for all aforementioned models in the same format as in Figure 5 for MHD. As before, $\overline{\Delta B_z}$ represents the model error on B_z, averaged over the THEMIS satellites that were conjugate with each IB observation. The conjugate THEMIS satellites were selected as described in Section 2. It is apparent that all models except for TS05 exhibit a common K vs. $\overline{\Delta B_z}$ dependence. It can be seen that T96 and T01 show the best agreement with observations, based on their compartively low values of $\overline{\Delta B_z}$. TA16RBF shows the worst agreement, with observations systematically underestimating the B_Z values. The TS05 model produced unrealistically low K-values for 6 of 7 IBs. It can be speculated that the deviation of TS05 from the common dependence is a result of its narrow specification. Since it was fitted to storm-time observations, quiet periods perhaps comprised a negligible part of the data. For this reason, the TS05 model output is an extrapolation in the region of quiet external conditions. Equation 5 has been fit to the points of the plot, excluding TS05 due to the substantial number of outliers present, and the resulting fit curve is plotted in black. The y-axis intercept of this fit occurs at $K = K_0 = 2.6$, with a 95% confidence interval of [2.1, 3.2]. This is significantly lower than the $K_0 = 16$ obtained with SWMF. $K_0 = 2.6$ falls within the range expected for CSS, but is appreciably below $K_{crit} = 8$.

7 Comparison of empirical and MHD results

Comparing between Figures 5 and 6, large differences are apparent between the SWMF simulations and the empirical models. In a preliminary effort to account for the

influence of magnetic field errors $\overline{\Delta B_z}$, we fitted Equation 5 to each dataset and noted the y-axis intercepts, which provide an estimate for the average K in the absence of these errors. Even these values differed by nearly an order of magnitude between the SWMF simulations and the empirical models. This indicates a significant difference in the dependency between K and B_z between the different models. One possible reason for this is a systematic difference in R_c within the current sheet, which depends on the model current sheet thickness. Given the sparsity of the available observational data, we have no means to determine the true value of R_c. However, the THEMIS configuration allows a rough estimation of $G = \frac{dB_r}{dz}$, which appears in the denominator of Equation 3, and is a major contributor to the value of R_c. As was mentioned in Section 2, it is evident from Figures 2c and 2d that THEMIS A and E are closely spaced in the x and y directions but are significantly displaced in the z direction. This enables us to estimate G as

$$G \approx \frac{B_{r_{THE}} - B_{r_{THA}}}{z_{THE} - z_{THA}}, \tag{6}$$

where the subscripts THA and THE refer to the spacecraft THEMIS A and E, and the values z_{THA} and z_{THE} refer to the GSM z coordinates of the spacecraft.

To test the validity of this estimate, we define

$$\Delta r_{xy_{E-A}} = \sqrt{(x_{THE} - x_{THA})^2 + (y_{THE} - y_{THA})^2} \tag{7}$$

and

$$\Delta z_{E-A} = z_{THE} - z_{THA}, \tag{8}$$

where again the positions are given in GSM coordinates and the subscripts THA and THE refer to the spacecraft THEMIS A and E. By taking the satellite positions at the seven selected IB observations shown in Table 1, we find that the ratio $\frac{\Delta z_{E-A}}{\Delta r_{xy_{E-A}}}$ ranges from 1.44 and 2.3, indicating that the displacement in z is consistently greater than the horizontal displacement $\Delta r_{xy_{E-A}}$. The ratio 1.44 not ideal since it indicates the horizontal distance between the spacecraft is significant compared with their displacement in z. This may contribute to the uncertainty in estimates of G, since any horizontal (x or y) gradient in B_r will influence the estimate of G. Another source of uncertainty is the distance of the

Figure 7. Observed B_r and B_z (GSM) for THEMIS A and E. IB crossing times are denoted with vertical dashed lines. Both spacecraft had an elliptical orbit with apogee around 11 R_E from the Earth, but the THEMIS A spacecraft was located approximately 1 R_E southward at apogee relative to THEMIS E.

spacecraft from the center of the current sheet, since we will apply this G estimation to correct K estimations computed in the current sheet.

To obtain reasonable estimates for G, we need B_r to differ appreciably between the THEMIS A and E spacecraft. Figure 7 shows the observed B_r and B_z magnetic field components at THEMIS A and E. Both spacecraft observed positive B_r, indicating that they are south of the current sheet. However, the B_r component is comparatively weak (<10 nT around apogee) at THEMIS E, while it is 15-20 nT greater at THEMIS A. This indicates that THEMIS E was located fairly close to the current sheet (for most of the day), while THEMIS A was farther below it. For the last IB crossing (16:54 UT), the B_r component at THEMIS E is 30.0 nT, significantly stronger than for the earlier IB crossings, indicating a more significant displacement from the current sheet. However, even for the 16:54 UT IB crossing the field at THEMIS E is still significantly weaker (by 11.6 nT) than that observed by THEMIS A at that time. It is worth noting that B_z also differs significantly between the two spacecraft. This means that the configuration is not 1-D. In a 1-D magnetic field (one in which $\frac{d\mathbf{B}}{dx} = \frac{d\mathbf{B}}{dy} = 0$), B_z cannot vary with z without violating $\nabla \cdot \mathbf{B} = 0$. While the current sheet can sometimes be approximately 1-D, the fact that B_z varies with z in the THEMIS observations implies that gradients in x and y are present, which will contribute to errors in estimating G.

The SWMF and empirical model results are shown together in Figure 8. Like Figures 5 and 6, Figure 8 shows K plotted as a function of $\overline{\Delta B_z}$. However, the points are now colored according to $\Delta G = G_{model} - G_{obs}$. For both the observations and the models, we estimate G using the difference between the THEMIS A and THEMIS E locations according to Equation 6. As shown in Figure 2, the two spacecraft were located relatively close in GSM x, but were displaced in z, and this resulted in significantly different B_r components as shown in Figure 7.

Fits to the SWMF points and the empirical model points (the same fits shown in Figures 5 and 6) are drawn in black in Figure 8. It is apparent that the simulations and

Figure 8. Estimated K as a function of $\overline{\Delta B_z}$ for the SWMF simulations (except SWMFb) and the empirical models (except TS05). Colors denote ΔG, the estimation error in the derivative $G = \frac{dB_r}{dz}$. Black lines denote least-squares fits to the SWMF simulations and empirical models.

empirical models are producing distinctly different results, with the SWMF consistently producing higher K values. At the same time, the emprical models tend to overestimate G, while the SWMF simulations tend to underestimate G. From Equation 3 we expect that overestimations of G will lead to smaller K values, and vice versa. Thus, the systematic underestimation of G by SWMF contributes to its comparatively large K estimates, and the systematic overestimation of G by the empirical models contributes to their smaller K estimates.

We now attempt to correct the K estimates based on the available observations. We first apply a correction for $\overline{\Delta B_z}$ using the same procedure used in *Dubyagin et al.* [2018]. Equation 5 provides an average relationship between K and $\overline{\Delta B_z}$ for each of the two classes of models (MHD and empirical). We use this relationship to correct particular K values by replacing the fitted y-axis intercept A_1 with a value $\log K^*$, where K^* is the value for a particular K that would be computed in the absence of B_z error, assuming the linear relationship of Equation 5 holds. This produces the relationship

$$\log K = \log K^* + A_2 \overline{\Delta B_z}, \tag{9}$$

from which we compute K^* as

$$K^* = K \exp(-A_2 \overline{\Delta B_z}). \tag{10}$$

Furthermore, motivated by the trends in G noted in Figure 8, we construct a new linearization of Equation 3, incorporating both $\overline{\Delta B_z}$ and ΔG:

$$\log K = C_1 + C_2 \overline{\Delta B_z} + C_3 \Delta G. \tag{11}$$

C_1, C_2, and C_3 are obtained using least squares minimization using all of the points shown in Figure 8 (that is, the output from SWMFa, SWMFc, and all the empirical mod-

els except TS05). Solving this equation for K in the case of $\overline{\Delta B_z} = \Delta G = 0$ gives $K_0 = \exp(C_1) = 6.0$ with a 95% confidence interval of [4.7, 7.8]. This can be regarded as an average corrected K for the case of zero magnetic field error. It falls within the expected range for CSS, but somewhat below the $K_{crit} = 8$ threshold.

For the general case (non-zero field error), we obtain a new correction K^{**}, which we derive from Equation 11 by substituting K^{**} for C_1 giving

$$\log K = \log K^{**} + C_2\overline{\Delta B_z} + C_3\Delta G, \tag{12}$$

which we can solve for K^{**} to obtain

$$K^{**} = K \exp(-C_2\overline{\Delta B_z} - C_3\Delta G). \tag{13}$$

Figure 9 shows the overall effect of applying these two correction schemes. The figure shows probability density functions (PDFs) of K, K^*, and K^{**}, obtained through kernel density estimation [*Parzen*, 1962]. Kernel density estimation approximates a PDF as a sum of Gaussian kernel functions centered at each data point. The resulting plot can be interpreted as a normalized histogram. The mean, median, and interquartile range (IQR) of the distributions shown in Figure 9 can be found in Table 2, along with the y-axis intercepts (with 95% confidence intervals) of the fits used to compute K^* and K^{**}. Figure 9a shows PDFs of K for SWMFa and SWMFc, and for all empirical models except TS05. The two distributions overlap negligibly, with the SWMF K values uniformly greater than those of the empirical models. Figure 9b shows PDFs of K^*, with the fit to Equation 5 having been performed separately for the empirical models and for SWMF. This correction leads to both distributions becoming more narrow. The many small K values of the empirical models are shifted higher, while many of the larger SWMF values are shifted down. There is still no overlap between the two distributions, however. Figure 9c shows PDFs of K^{**}. The two classes of models did not individually have a clear linear relationship between K and G, so to compute K^{**} a single fit was performed for all models together, once again omitting TS05 and SWMFb. Some overlap can be seen in the distributions of K^{**} in Figure 9c, although the corresponding interquartile ranges shown in Table 2 for K^{**} do not overlap.

Figure 9. Kernel density plots of (a) K, (b) K^*, and (c) K^{**} for SWMFa, SWMFb, and for all empirical models except TS05.

Model type	25th percentile	Median	75th percentile	y-axis intercept	Intercept 95% CI
			Uncorrected K		
SWMF	18	21	27	–	–
Empirical	0.93	2.3	4.6	–	–
Both	1.2	4.3	17	–	–
			K^* correction		
SWMF	14	15	19	16	[13, 19]
Empirical	2.0	2.8	3.7	2.6	[2.1, 3.2]
Both	2.5	3.5	13	–	–
			K^{**} correction		
SWMF	7.6	9.9	11	6.0	[4.7, 7.8]
Empirical	4.4	5.4	7.6	6.0	[4.7, 7.8]
Both	4.7	6.2	9.5	6.0	[4.7, 7.8]

Table 2. Summary of the results of the correction schemes. The 25th percentile, median, and 75th percentile are shown for K, K^*, and K^{**}. For K^* and K^{**} the y-axis intercept (i.e., the correction value for the special case of $\overline{\Delta B_z} = \Delta G = 0$) and its 95% confidence interval are shown. Note that in the case of K^{**} the y-axis intercept is the same for both SWMF and empirical models since a fit is obtained by fitting to both types of models simultaneously and the same fit is used to correct both types of models.

8 Discussion and conclusions

The goal of this study is to test the viability of using MHD for estimating K values associated with IB observations, and to provide better constraints on the range of K associated with the IB during quiet time. To accomplish this, we used multiple models, both physics-based and empirical, to compute K values corresponding to IB observations. We ran three SWMF simulations using different simulation parameters, as well as six different empirical models. We used the same time interval and the same IB observations that were used by *Ilie et al.* [2015]. A quiet interval was chosen in order to reduce the chance of particle scattering due to wave-particle interactions, which occur primarily during active periods [*Bräysy et al.*, 1998; *Halford et al.*, 2010; *Usanova et al.*, 2012], and to reduce possible inaccuracies in the model mapping. In addition, *Ilie et al.* [2015] noted an absence of observational evidence for EMIC waves during the interval chosen. We first traced fields from the locations where the IB was observed through the magnetic fields of each model. We computed K at the point of minimum $|B|$ along each of these field lines. However, this computed K is still subject to errors in the model field relative to reality. To address this, we corrected each K value based on the error in B relative to observations by nearby THEMIS spacecraft. By computing K with multiple models, and correcting for the errors in those models, we are able to better constrain the possible range of K associated with CSS driven IB formation, and to test the hypothesis that these quiet-time IB observations are associated with CSS.

Comparison between the SWMF simulations and in situ observations indicates a tendency toward an under-stretched night side magnetic field geometry in the simulations. This same tendency was reported in *Ilie et al.* [2015] for the same event with SWMF, and other previous papers have also reported under-stretched fields with MHD [e.g. *Welling and Ridley*, 2010; *Ganushkina et al.*, 2010], though this can be reduced through the use of non-ideal MHD [e.g. *Meng et al.*, 2013]. The empirical models exhibited a range of behaviors in terms of magnetotail stretching: The T01 fields tend to be under-stretched and the TS05, TA16RBF, and TA15N fields are consistently over-stretched, while the T96 and TA15B fields are sometimes over-stretched and sometimes under-stretched. This reflects a variety of observational datasets used to construct the models, as well as different strategies used for fitting. There has been some evolution in terms of field stretching in empirical models. The T96 model has been previously reported as producing over-stretched fields, but the over-stretching was most pronounced during disturbed periods

[*Tsyganenko*, 2001; *Ganushkina et al.*, 2002; *Huang et al.*, 2008]. *Huang et al.* [2008] reported TS05 as producing less field stretching than T96, but this was for a storm interval and at closer distances than our THEMIS observations. The fact that our results do not show this tendency in T96 may be due in part to the use of a quiet period for this study. The TA16RBF model was previously reported as having similar tail stretching as the older T89 model in the 10-12 R_E region [*Tsyganenko and Andreeva*, 2016], and T89 in turn has been reported as producing over-stretched fields in the magnetotail [*Tsyganenko*, 1989; *Peredo et al.*, 1993].

At the same time, the SWMF consistently produces negative values for ΔG, implying a thicker and/or weaker than actual current sheet. The empirical models, on the other hand, uniformly overestimate G, which implies a current sheet that is thinner and/or stronger than actual. The combined effect of the discrepancies in B_z and G is that the SWMF consistently produces large K values, while the empirical models generally produce smaller K.

The large range of K values we obtain, and their association with magnetic field errors, highlights the importance of quantifying the influence of magnetic field errors on the K estimates, as we did in computing K^* and K^{**}. However, it should be noted that K^* and K^{**} should be regarded as rough estimates of the true value of K. The corrections are subject to a number of sources of uncertainty. These include errors due to linearization of the nonlinear K formula, the position of the satellites relative to the $|B|_{min}$ point, and the fact that we perform linear fits of multiple models and multiple IB observations, effectively averaging them together. Estimations of the dependence of K on G are especially sensitive to the satellite positions, because G has a larger gradient in z (compared to B_z), and because the errors due to the positions of the spacecraft relative to the $|B|_{min}$ point are compounded by the errors contributed by the positions of the spacecraft relative to each other (on which the estimation of G depends). A more complex K correction that accounts for the position of the satellites relative to the $|B|_{min}$ point might be possible, but this could be error prone as it would require introducing new assumptions about the variation of B_r and B_z with position. It is possible that some effects of the relative distances and directions to spacecraft are somehow corrected for as a result of the fitting process used to obtain the correction factors, but this is by no means certain. A final source of uncertainty is the fact that we include only the G and B_z contributions in the correction of

K. Including additional field components would likely result in over-fitting given the small number of points used in our analysis, but might be appropriate for a larger scale study.

In addition, the criteria for selecting conjugate spacecraft may impact the estimations of G and B_z. One could conceive of alternate criteria, using either wider or narrower ranges in MLT or distance from the Earth, or using locations relative to the traced field lines as part of the selection criteria. The simple mean of ΔB_z over all conjugate spacecraft could also be replaced with another measure of central tendency, perhaps a weighted average applying higher weights to spacecraft that were closer to the field line mapping to the NOAA or METOP spacecraft. However, it is not obvious that the spacecraft closest to the mapped location will provide a better error estimate in practice, and *Dubyagin et al.* [2018] attempted several of these alternative methods and found no significant improvement in the correlation between K and ΔB_z.

Despite the aforementioned sources of uncertainty, the narrow range of values obtained for K^{**} (compared with the range of the uncorrected K), and the overlap between the two classes of models, indicate that the procedure is largely successful in accounting for the influence of magnetic field errors on K estimates in the models. This means that both B_z and $G = \frac{dB_r}{dz}$ contribute significantly to errors in estimating K, and that the two corrections in combination account for a large fraction of the variation in model K estimations.

The relatively narrow ranges we obtained for K^{**} also suggests that the IB events we analyzed were formed by a common mechanism which depends primarily on field geometry. A majority of the K^{**} values (53% for SWMF, and 91% for the empirical models) are below $K = 10$, which implies that CSS is the likely mechanism forming the IB in these cases. The fact that we obtain this using two classes of models, with very different underlying assumptions, lends additional confidence to this result. By comparing the IQR we obtained for K with the results of *Ilie et al.* [2015], we find that our results and systematically smaller, and slightly more tightly distributed, than those obtained by *Ilie et al.* [2015] for the same event. The IQR of K was 30-42 in the data reported by *Ilie et al.* [2015]; the fact that this range does not overlap with the IQR of our data indicates that the difference between their results and ours is larger than the degree of variation within each dataset. That we obtain smaller values of K over a narrower range compared with *Ilie et al.* [2015] indicates that more accurate dipole parameters and other changes to the simulation set-

tings had a substantial effect. We obtain a much narrower IQR for K^{**}, indicating that a large part of the variation in SWMF-derived K can be attributed to correctible errors in the model's magnetic field estimation, rather than to differences in the IB formation process over time. The range of K^{**} is also narrower than the range of K values obtained by *Sergeev et al.* [2015b]. In the present work we aimed to only study IB's that were likely to have been formed by CSS. To that end we chose a quiet-time interval, checked for the absence of EMIC wave observations, and only used events that had typical appearance. *Sergeev et al.* [2015b] studied a longer time period which was mostly, but not exclusively, quiet time. Since they do not describe any special efforts to restrict their analysis to "typical" IB observations, it is likely they used all available events that were conjugate with THEMIS spacecraft. Since *Sergeev et al.* [2015b] used adaptive models that attempted to minimize the magnetic field error relative to the THEMIS observations, the fact that we obtain a narrower range for K^{**} is likely due to the use of a longer time period, more IB observations, and a wider range of conditions in *Sergeev et al.* [2015b] compared to the present work.

The $K = 6.0$ value we obtained is marginally lower than the commonly used $K_{crit} = 8$ threshold. Since the $K_{crit} = 8$ is outside the 95% confidence interval for K, our result is significantly lower in a statistical sense. However, this result depends on the use of both the SWMF and the empirical models together in the fit. The y-axis intercept values in the fourth and fifth rows of Table 2 (2.6 for the empirical models and 16 for SWMF) can be regarded as probable lower and upper bounds for the range of variability that could result if we changed the mixture of models used in the study. That is, we would expect the intercept for the combined K estimate (using all models together) to range from roughly 2.6 to roughly 16 if we were to modify the mix of models included in the K^{**} correction.

Our work shows that even after restricting the analysis to a few quiet-time IB observations with ideal spatial distribution of fluxes across the IB, and after correcting the results for errors in the magnetic field models, a substantial uncertainty remains in the range of K. The remaining uncertainty is consistent with the dependency on the incident particle population reported by *Delcourt et al.* [1996], so there is no need to invoke an additional scattering mechanism to explain it. Therefore, obtaining a more precise threshold condition than the range we obtained will likely require not only an improved magnetic field model but also an accounting for the phase space distribution of particles prior to scattering.

The conclusions of the paper can be summarized as follows:

1. Prior to correction, the MHD simulations often (though not always) produce K values above the expected range for CSS, while the empirical models produce K values at the low end of the expected range for CSS.
2. The corrected K^* and K^{**} values have much narrower spread than the uncorrected K values. This implies that much of the spread in K was due to errors in the estimated magnetic field, but also shows that these errors can be corrected.
3. The distributions of K^{**} overlap substantially for the MHD and for the empirical models.
4. A majority of the corrected K^{**} values (53% for SWMF, and 91% for the empirical models) fall within the expected range for CSS, which supports the hypothesis that the IB was formed by CSS in those cases.
5. We estimate K_0, the average value of K in the absence of magnetic field error, to be 6.0. This is within the expected range for CSS, and somewhat lower than $K_{crit} = 8$. However, the uncertainty range is estimated as [2.6, 16], which extends above $K_{crit} = 8$.

Acknowledgments

The research of S. Dubyagin and N. Ganushkina leading to these results was partly funded by the European Union's Horizon 2020 research and innovation programme under grand agreement 637302 PROGRESS. The work of N. Ganushkina and J. Haiducek in Michigan was also partly supported by the National Aeronautics and Space Administration under grant agreements NNX14AF34G, NNX17AB87G and 80NSS17K0015 issued through the ROSES-2013 and ROSES-2016 programmes. Portions of the results presented here were achieved under the framework of the Finnish Centre of Excellence in Research of Sustainable Space (FORESAIL) funded by the Academy of Finland, decision number 312351.

The NOAA/POES particle data were downloaded form National Geophysical Data Center website: https://www.ngdc.noaa.gov/stp/ satellite/poes/index.html.

THEMIS magnetic field data were loaded and calibrated using official software at http://themis.ssl.berkeley.edu.

GOES magnetic field data were obtained from CDAWeb (https://cdaweb.sci.gsfc.nasa.gov/).

The precomputed input parameters for the empirical models were downloaded from http://geo.phys.spbu.ru/~tsyganenko/modeling.html.

Full output from the three model runs presented in this paper can be found at the following URLs:

http://vmr.engin.umich.edu/Model/_swmf_mag/plot?run=IB_quiet_feb2009_SWMFa
http://vmr.engin.umich.edu/Model/_swmf_mag/plot?run=IB_quiet_feb2009_SWMFb
http://vmr.engin.umich.edu/Model/_swmf_mag/plot?run=IB_quiet_feb2009_SWMFc

References

Alfvén, H., and C. G. Fälthammar (1963), *Cosmical electrodynamics: Fundamental Principles (Volume 1)*, International series of monographs on physics, Clarendon Press.

Asikainen, T., K. Mursula, and V. Maliniemi (2012), Correction of detector noise and recalibration of NOAA/MEPED energetic proton fluxes, *Journal of Geophysical Research: Space Physics*, *117*(A9), A09,204, doi:10.1029/2012JA017593.

Auster, H. U., K. H. Glassmeier, W. Magnes, O. Aydogar, W. Baumjohann, D. Constantinescu, D. Fischer, K. H. Fornacon, E. Georgescu, P. Harvey, O. Hillenmaier, R. Kroth, M. Ludlam, Y. Narita, R. Nakamura, K. Okrafka, F. Plaschke, I. Richter, H. Schwarzl, B. Stoll, A. Valavanoglou, and M. Wiedemann (2008), The THEMIS Fluxgate Magnetometer, *Space Science Reviews*, *141*(1-4), 235–264, doi:10.1007/s11214-008-9365-9.

Baker, K. B., and S. Wing (1989), A new magnetic coordinate system for conjugate studies at high latitudes, *Journal of Geophysical Research: Space Physics*, *94*(A7), 9139–9143, doi:10.1029/JA094IA07P09139.

Borovsky, J. E., and K. Yakymenko (2017), Substorm occurrence rates, substorm recurrence times, and solar wind structure, *Journal of Geophysical Research: Space Physics*, *122*(3), 2973–2998, doi:10.1002/2016JA023625.

Boynton, R. J., M. A. Balikhin, S. A. Billings, H. L. Wei, and N. Ganushkina (2011), Using the NARMAX OLS-ERR algorithm to obtain the most influential coupling functions that affect the evolution of the magnetosphere, *Journal of Geophysical Research: Space Physics*, *116*(A5), A05,218, doi:10.1029/2010JA015505.

Bräysy, T., K. Mursula, and G. Marklund (1998), Ion cyclotron waves during a great magnetic storm observed by Freja double-probe electric field instrument, *Journal of Geo-*

physical Research: Space Physics, *103*(A3), 4145–4155, doi:10.1029/97JA02820.

Büchner, J., and L. M. Zelenyi (1987), Chaotization of the electron motion as the cause of an internal magnetotail instability and substorm onset, *Journal of Geophysical Research*, *92*(A12), 13,456–13,466, doi:10.1029/JA092iA12p13456.

Chen, J., and P. J. Palmadesso (1986), Chaos and Nonlinear Dynamics of Single-Particle Orbits in a Magnetotaillike Magnetic Field, *Journal of Geophysical Research*, *91*(1), 1499–1508, doi:10.1029/JA091iA02p01499.

Coroniti, F. V. (1980), On the tearing mode in quasi-neutral sheets, *Journal of Geophysical Research*, *85*(A12), 6719, doi:10.1029/JA085iA12p06719.

Delcourt, D. C., J.-A. Sauvaud, R. F. Martin, and T. E. Moore (1996), On the nonadiabatic precipitation of ions from the near-Earth plasma sheet, *Journal of Geophysical Research: Space Physics*, *101*(A8), 17,409–17,418, doi:10.1029/96JA01006.

Delcourt, D. C., T. E. Moore, B. L. Giles, and M.-C. Fok (2000), Quantitative modeling of modulated ion injections observed by Polar-Thermal Ion Dynamics Experiment in the cusp region, *Journal of Geophysical Research: Space Physics*, *105*(A11), 25,191–25,203, doi:10.1029/2000JA000034.

Delcourt, D. C., H. V. Malova, and L. M. Zelenyi (2006), Quasi-adiabaticity in bifurcated current sheets, *Geophysical Research Letters*, *33*(6), L06,106, doi: 10.1029/2005GL025463.

DeZeeuw, D. L., T. I. Gombosi, C. P. T. Groth, K. G. Powell, and Q. F. Stout (2000), An Adaptive MHD Method for Global Space Weather Simulations, *IEEE Trans. Plasma Sci.*, *28*(6), 1956–1965, doi:10.1109/27.902224.

Dubyagin, S., N. Ganushkina, S. Apatenkov, M. Kubyshkina, H. Singer, and M. Liemohn (2013), Geometry of duskside equatorial current during magnetic storm main phase as deduced from magnetospheric and low-altitude observations, *Annales Geophysicae*, *31*(3), 395–408, doi:10.5194/angeo-31-395-2013.

Dubyagin, S., N. Y. Ganushkina, and V. Sergeev (2018), Formation of 30 KeV Proton Isotropic Boundaries During Geomagnetic Storms, *Journal of Geophysical Research: Space Physics*, doi:10.1002/2017JA024587.

Evans, D. S., and M. S. Greer (2000), Polar Orbiting Environmental Satellite Space Environment Monitor -2 Instrument Descriptions and Archive Data Documentation, *Tech. rep.*, Boulder, Colorado.

Ganushkina, N. Y., T. I. Pulkkinen, M. V. Kubyshkina, H. J. Singer, and C. T. Russell (2002), Modeling the ring current magnetic field during storms, *Journal of Geophysical Research*, *107*(A7), 1092, doi:10.1029/2001JA900101.

Ganushkina, N. Y., T. I. Pulkkinen, M. V. Kubyshkina, V. A. Sergeev, E. A. Lvova, T. A. Yahnina, A. G. Yahnin, T. Fritz, N. Yu Ganushkina, T. I. Pulkkinen, M. V. Kubyshkina, V. A. Sergeev, E. A. Lvova, T. A. Yahnina, A. G. Yahnin, and T. Fritz (2005), Proton isotropy boundaries as measured on mid- and low-altitude satellites, *Annales Geophysicae*, *23*(5), 1839–1847, doi:10.5194/angeo-23-1839-2005.

Ganushkina, N. Y., M. W. Liemohn, M. V. Kubyshkina, R. Ilie, and H. J. Singer (2010), Distortions of the magnetic field by storm-time current systems in Earth's magnetosphere, *Annales Geophysicae*, *28*(1), 123–140, doi:10.5194/angeo-28-123-2010.

Gilson, M. L., J. Raeder, E. Donovan, Y. S. Ge, and L. Kepko (2012), Global simulation of proton precipitation due to field line curvature during substorms, *Journal of Geophysical Research: Space Physics*, *117*(A5), A05,216, doi:10.1029/2012JA017562.

Gvozdevsky, B. B., V. A. Sergeev, and K. Mursula (1997), Long lasting energetic proton precipitation in the inner magnetosphere after substorms, *Journal of Geophysical Research: Space Physics*, *102*(A11), 24,333–24,338, doi:10.1029/97JA02062.

Haiducek, J. D., D. T. Welling, N. Y. Ganushkina, S. K. Morley, and D. S. Ozturk (2017), SWMF Global Magnetosphere Simulations of January 2005: Geomagnetic Indices and Cross-Polar Cap Potential, *Space Weather*, *15*(12), 1567–1587, doi:10.1002/2017SW001695.

Halford, A. J., B. J. Fraser, and S. K. Morley (2010), EMIC wave activity during geomagnetic storm and nonstorm periods: CRRES results, *Journal of Geophysical Research: Space Physics*, *115*(A12), A12,248, doi:10.1029/2010JA015716.

Huang, C.-L., H. E. Spence, H. J. Singer, and N. A. Tsyganenko (2008), A quantitative assessment of empirical magnetic field models at geosynchronous orbit during magnetic storms, *Journal of Geophysical Research: Space Physics*, *113*(A4), n/a–n/a, doi:10.1029/2007JA012623.

Hultqvist, B. (1979), The hot ion component of the magnetospheric plasma and some relations to the electron component-observations and physical implications, *Space Science Reviews*, *23*(4), 581–675, doi:10.1007/BF00212357.

Ilie, R., N. Ganushkina, G. Toth, S. Dubyagin, and M. W. Liemohn (2015), Testing the magnetotail configuration based on observations of low-altitude isotropic boundaries

914 during quiet times, *Journal of Geophysical Research: Space Physics*, *120*(12), 10,557–
915 10,573, doi:10.1002/2015JA021858.

916 Imhof, W. L., J. B. Reagan, and E. E. Gaines (1977), Fine-scale spatial structure in the
917 pitch angle distributions of energetic particles near the midnight trapping boundary,
918 *Journal of Geophysical Research*, *82*(32), 5215–5221, doi:10.1029/JA082i032p05215.

919 Kennel, C. F., and H. E. Petschek (1966), Limit on stably trapped particle fluxes, *Journal*
920 *of Geophysical Research*, *71*(1), 1–28, doi:10.1029/JZ071i001p00001.

921 Liang, J., E. Donovan, B. Ni, C. Yue, F. Jiang, and V. Angelopoulos (2014), On an
922 energy-latitude dispersion pattern of ion precipitation potentially associated with mag-
923 netospheric EMIC waves, *Journal of Geophysical Research: Space Physics*, *119*(10),
924 8137–8160, doi:10.1002/2014JA020226.

925 Lyons, L. R., and T. W. Speiser (1982), Evidence for current sheet acceleration
926 in the geomagnetic tail, *Journal of Geophysical Research*, *87*(A4), 2276, doi:
927 10.1029/JA087iA04p02276.

928 Meng, X., G. Tóth, A. Glocer, M.-C. Fok, and T. I. Gombosi (2013), Pressure anisotropy
929 in global magnetospheric simulations: Coupling with ring current models, *Journal of*
930 *Geophysical Research: Space Physics*, *118*(9), 5639–5658, doi:10.1002/jgra.50539.

931 Meurant, M., J.-C. Gérard, C. Blockx, E. Spanswick, E. F. Donovan, B. Hubert,
932 V. Coumans, and M. Connors (2007), EL - a possible indicator to monitor the mag-
933 netic field stretching at global scale during substorm expansive phase: Statistical
934 study, *Journal of Geophysical Research: Space Physics*, *112*(A5), A05,222, doi:
935 10.1029/2006JA012126.

936 Montgomery, D. C., E. A. Peck, and G. G. Vining (2012), *Introduction to linear regression*
937 *analysis*, 645 pp., Wiley.

938 Newell, P. T., and J. W. Gjerloev (2011), Evaluation of SuperMAG auroral electrojet in-
939 dices as indicators of substorms and auroral power, *Journal of Geophysical Research:*
940 *Space Physics*, *116*(A12), A12,211, doi:10.1029/2011JA016779.

941 Newell, P. T., V. A. Sergeev, G. R. Bikkuzina, and S. Wing (1998), Characterizing the
942 state of the magnetosphere: Testing the ion precipitation maxima latitude (b2i) and the
943 ion isotropy boundary, *Journal of Geophysical Research: Space Physics*, *103*(A3), 4739–
944 4745, doi:10.1029/97JA03622.

945 Newell, P. T., T. Sotirelis, K. Liou, C.-I. Meng, and F. J. Rich (2007), A nearly univer-
946 sal solar wind-magnetosphere coupling function inferred from 10 magnetospheric

state variables, *Journal of Geophysical Research: Space Physics*, *112*(A1), doi: 10.1029/2006JA012015.

Parzen, E. (1962), On estimation of a probability density function and mode, *Ann. Math. Statist.*, *33*(3), 1065–1076, doi:10.1214/aoms/1177704472.

Peredo, M., D. P. Stern, and N. A. Tsyganenko (1993), Are existing magnetospheric models excessively stretched?, *Journal of Geophysical Research*, *98*(A9), 15,343, doi: 10.1029/93JA01150.

Powell, K. G., P. L. Roe, T. J. Linde, T. I. Gombosi, and D. L. De Zeeuw (1999), A Solution-Adaptive Upwind Scheme for Ideal Magnetohydrodynamics, *Journal of Computational Physics*, *154*(2), 284–309, doi:10.1006/jcph.1999.6299.

Ridley, A. J., and M. W. Liemohn (2002), A model-derived storm time asymmetric ring current driven electric field description, *Journal of Geophysical Research: Space Physics*, *107*(A8), SMP 2–1–SMP 2–12, doi:10.1029/2001JA000051.

Ridley, A. J., T. I. Gombosi, and D. L. De Zeeuw (2004), Ionospheric control of the magnetosphere: conductance, *Annales Geophysicae*, *22*(2), 567–584, doi:10.5194/angeo-22-567-2004.

Sazykin, S. Y. (2000), Theoretical Studies of Penetration of Magnetospheric Electric Fields to the Ionosphere, Ph.D. thesis, Utah State University, Logan, Utah.

Sergeev, V., and N. Tsyganenko (1982), Energetic particle losses and trapping boundaries as deduced from calculations with a realistic magnetic field model, *Planetary and Space Science*, *30*(10), 999–1006, doi:10.1016/0032-0633(82)90149-0.

Sergeev, V., E. Sazhina, N. Tsyganenko, J. Lundblad, and F. Søraas (1983), Pitch-angle scattering of energetic protons in the magnetotail current sheet as the dominant source of their isotropic precipitation into the nightside ionosphere, *Planetary and Space Science*, *31*(10), 1147–1155, doi:10.1016/0032-0633(83)90103-4.

Sergeev, V. A., and B. B. Gvozdevsky (1995), MT-index – a possible new index to characterize the magnetic configuration of magnetotail, *Annales Geophysicae*, *13*(10), 1093–1103, doi:10.1007/s00585-995-1093-9.

Sergeev, V. A., M. Malkov, and K. Mursula (1993), Testing the isotropic boundary algorithm method to evaluate the magnetic field configuration in the tail, *Journal of Geophysical Research: Space Physics*, *98*(A5), 7609–7620, doi:10.1029/92JA02587.

Sergeev, V. A., T. A. Kornilova, I. A. Kornilov, V. Angelopoulos, M. V. Kubyshkina, M. Fillingim, R. Nakamura, J. P. McFadden, and D. Larson (2010), Auroral signatures

of the plasma injection and dipolarization in the inner magnetosphere, *Journal of Geophysical Research: Space Physics*, *115*(A2), A02,202, doi:10.1029/2009JA014522.

Sergeev, V. A., S. A. Chernyaeva, S. V. Apatenkov, N. Y. Ganushkina, and S. V. Dubyagin (2015a), Energy-latitude dispersion patterns near the isotropy boundaries of energetic protons, *Annales Geophysicae*, *33*(8), 1059–1070, doi:10.5194/angeo-33-1059-2015.

Sergeev, V. A., I. A. Chernyaev, V. Angelopoulos, and N. Y. Ganushkina (2015b), Magnetospheric conditions near the equatorial footpoints of proton isotropy boundaries, *Annales Geophysicae*, *33*(12), 1485–1493, doi:10.5194/angeo-33-1485-2015.

Singer, H., L. Matheson, R. Grubb, A. Newman, and D. Bouwer (1996), Monitoring space weather with the GOES magnetometers, in *Proceedings of SPIE*, vol. 2812, edited by E. R. Washwell, pp. 299–308, International Society for Optics and Photonics, doi: 10.1117/12.254077.

Søraas, F. (1972), ESRO IA/B Observations at High Latitudes of Trapped and Precipitating Protons with Energies above 100 keV, in *Earth's Magnetospheric Processes*, pp. 120–132, Springer, Dordrecht, doi:10.1007/978-94-010-2896-7_12.

Søraas, F., J. Lundblad, N. Maltseva, V. Troitskaya, and V. Selivanov (1980), A comparison between simultaneous I.P.D.P. groundbased observations and observations of energetic protons obtained by satellites, *Planetary and Space Science*, *28*(4), 387–405, doi: 10.1016/0032-0633(80)90043-4.

Tapping, K. F. (2013), The 10.7 cm solar radio flux (F 10.7), *Space Weather*, *11*(7), 394–406, doi:10.1002/swe.20064.

Toffoletto, F., S. Sazykin, R. Spiro, and R. Wolf (2003), Inner magnetospheric modeling with the Rice Convection Model, *Space Sci. Rev.*, *107*(1-2), 175–196, doi: 10.1023/A:1025532008047.

Tóth, G., I. V. Sokolov, T. I. Gombosi, D. R. Chesney, C. R. Clauer, D. L. De Zeeuw, K. C. Hansen, K. J. Kane, W. B. Manchester, R. C. Oehmke, K. G. Powell, A. J. Ridley, I. I. Roussev, Q. F. Stout, O. Volberg, R. A. Wolf, S. Sazykin, A. Chan, B. Yu, and J. Kóta (2005), Space Weather Modeling Framework: A new tool for the space science community, *Journal of Geophysical Research: Space Physics*, *110*(A12), doi: 10.1029/2005JA011126.

Tsyganenko, N. A. (1982), Pitch-angle scattering of energetic particles in the current sheet of the magnetospheric tail and stationary distribution functions, *Planetary and Space Science*, *30*(5), 433–437, doi:10.1016/0032-0633(82)90052-6.

Tsyganenko, N. A. (1989), A magnetospheric magnetic field model with a warped tail current sheet, *Planetary and Space Science*, *37*(1), 5–20, doi:10.1016/0032-0633(89)90066-4.

Tsyganenko, N. A. (1995), Modeling the Earth's Magnetospheric Magnetic Field Confined Within a Realistic Magnetopause, *J. Geophys. Res.*, *100*(A4), 5599–5612, doi:10.1029/94JA03193.

Tsyganenko, N. A. (2001), Empirical Magnetic Field Models for the Space Weather Program, pp. 273–280, American Geophysical Union (AGU), doi:10.1029/GM125p0273.

Tsyganenko, N. A. (2002), A model of the near magnetosphere with a dawn-dusk asymmetry 1. Mathematical structure, *Journal of Geophysical Research: Space Physics*, *107*(A8), SMP 12–1–SMP 12–15, doi:10.1029/2001JA000219.

Tsyganenko, N. A., and V. A. Andreeva (2015), A forecasting model of the magnetosphere driven by an optimal solar wind coupling function, *Journal of Geophysical Research: Space Physics*, *120*(10), 8401–8425, doi:10.1002/2015JA021641.

Tsyganenko, N. A., and V. A. Andreeva (2016), An empirical RBF model of the magnetosphere parameterized by interplanetary and ground-based drivers, *Journal of Geophysical Research: Space Physics*, *121*(11), 10,786–10,802, doi:10.1002/2016JA023217.

Tsyganenko, N. A., and M. I. Sitnov (2005), Modeling the dynamics of the inner magnetosphere during strong geomagnetic storms, *Journal of Geophysical Research*, *110*(A3), A03,208, doi:10.1029/2004JA010798.

Usanova, M. E., I. R. Mann, J. Bortnik, L. Shao, and V. Angelopoulos (2012), THEMIS observations of electromagnetic ion cyclotron wave occurrence: Dependence on AE, SYMH, and solar wind dynamic pressure, *Journal of Geophysical Research: Space Physics*, *117*(A10), A10,218, doi:10.1029/2012JA018049.

Welling, D. T., and A. J. Ridley (2010), Validation of SWMF magnetic field and plasma, *Space Weather*, *8*(3), S03,002, doi:10.1029/2009SW000494.

West, H. I., R. M. Buck, and M. G. Kivelson (1978), On the configuration of the magnetotail near midnight during quiet and weakly disturbed periods: Magnetic field modeling, *Journal of Geophysical Research*, *83*(A8), 3819, doi:10.1029/JA083iA08p03819.

Wolf, R. A., M. Harel, R. W. Spiro, G.-H. Voigt, P. H. Reiff, and C. K. Chen (1982), Computer simulation of inner magnetospheric dynamics for the magnetic storm of July 29, 1977, *Journal of Geophysical Research*, *87*(A8), 5949–5962, doi:10.1029/JA087iA08p05949.

Yahnin, A. G., and T. A. Yahnina (2007), Energetic proton precipitation related to ion-cyclotron waves, *Journal of Atmospheric and Solar-Terrestrial Physics*, *69*(14), 1690–1706, doi:10.1016/j.jastp.2007.02.010.

Young, D. T., H. Balsiger, and J. Geiss (1982), Correlations of magnetospheric ion composition with geomagnetic and solar activity, *Journal of Geophysical Research*, *87*(A11), 9077–9096, doi:10.1029/JA087iA11p09077.

Yue, C., C.-P. Wang, L. Lyons, J. Liang, E. F. Donovan, S. G. Zaharia, and M. Henderson (2014), Current sheet scattering and ion isotropic boundary under 3-D empirical force-balanced magnetic field, *Journal of Geophysical Research: Space Physics*, *119*(10), 8202–8211, doi:10.1002/2014JA020172.

Figure 1.

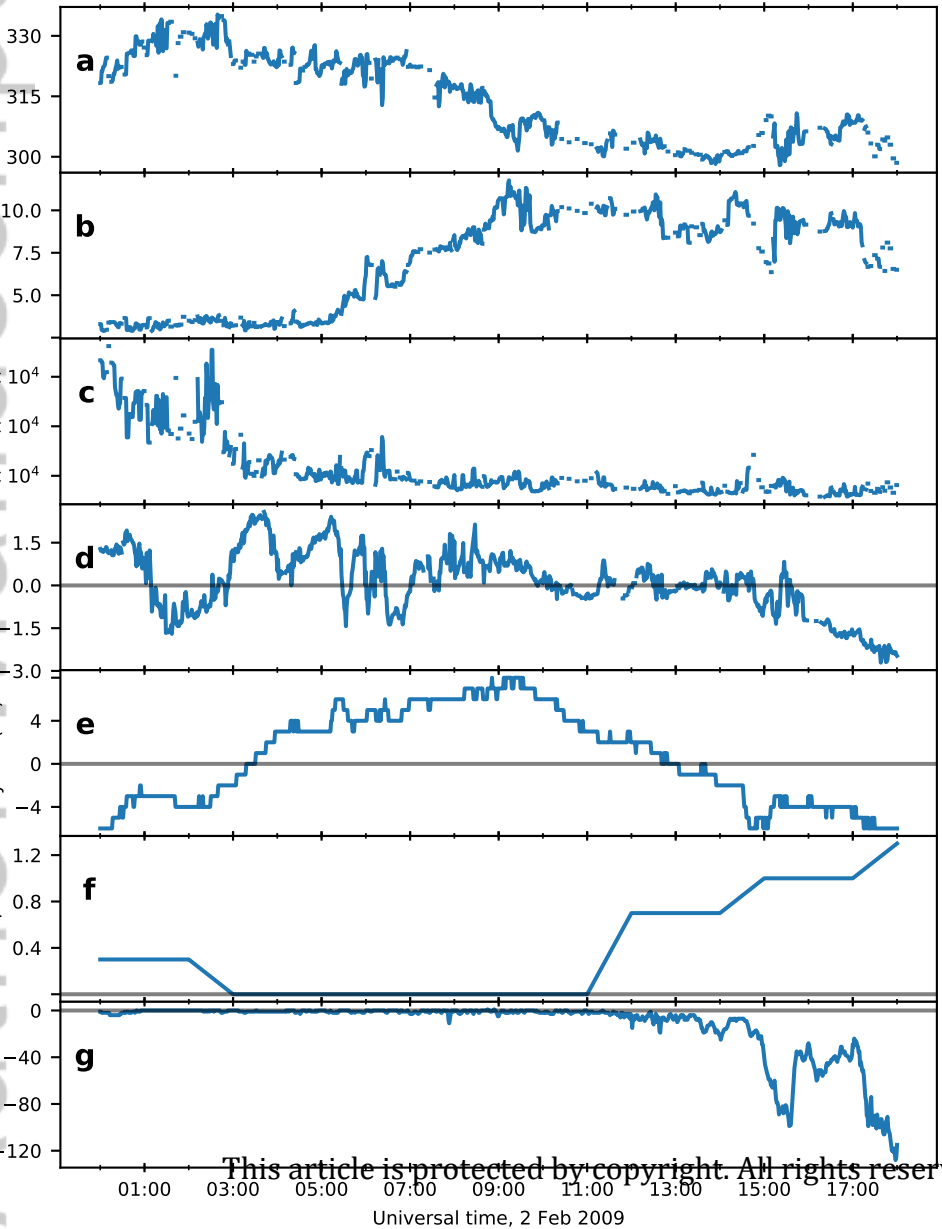

Figure 2.

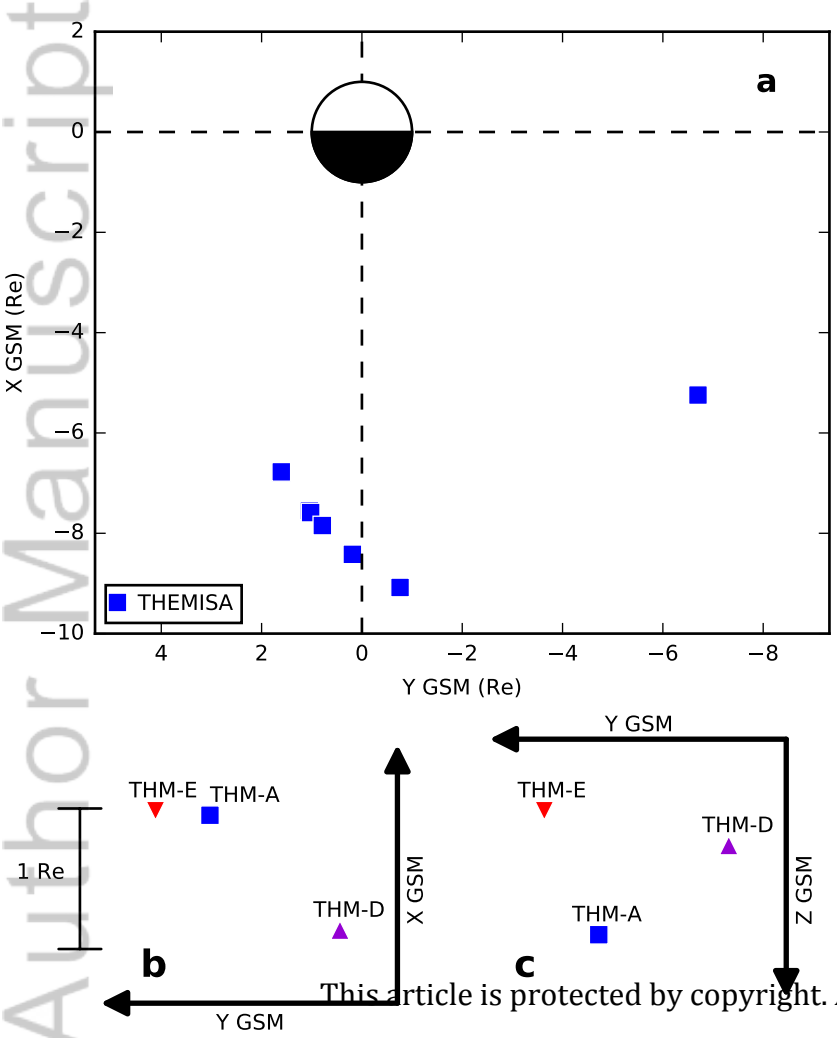

Figure 3.

UT	02:00	05:00	08:00	11:00	14:00	17:00	02:00	05:00	08:00	11:00	14:00	17:00
MLT	23.3	0.553	1.48	2.14	2.74	3.49	23.3	0.553	1.48	2.14	2.74	3.49
X GSM	-7.14	-9.4	-10.1	-9.51	-7.89	-5.14	-7.14	-9.4	-10.1	-9.51	-7.89	-5.14
Y GSM	1.37	-1.37	-4.09	-5.98	-6.97	-6.68	1.37	-1.37	-4.09	-5.98	-6.97	-6.68
Z GSM	-2.68	-3.91	-3.81	-3.17	-2.77	-2.49	-2.68	-3.91	-3.81	-3.17	-2.77	-2.49

Figure 4.

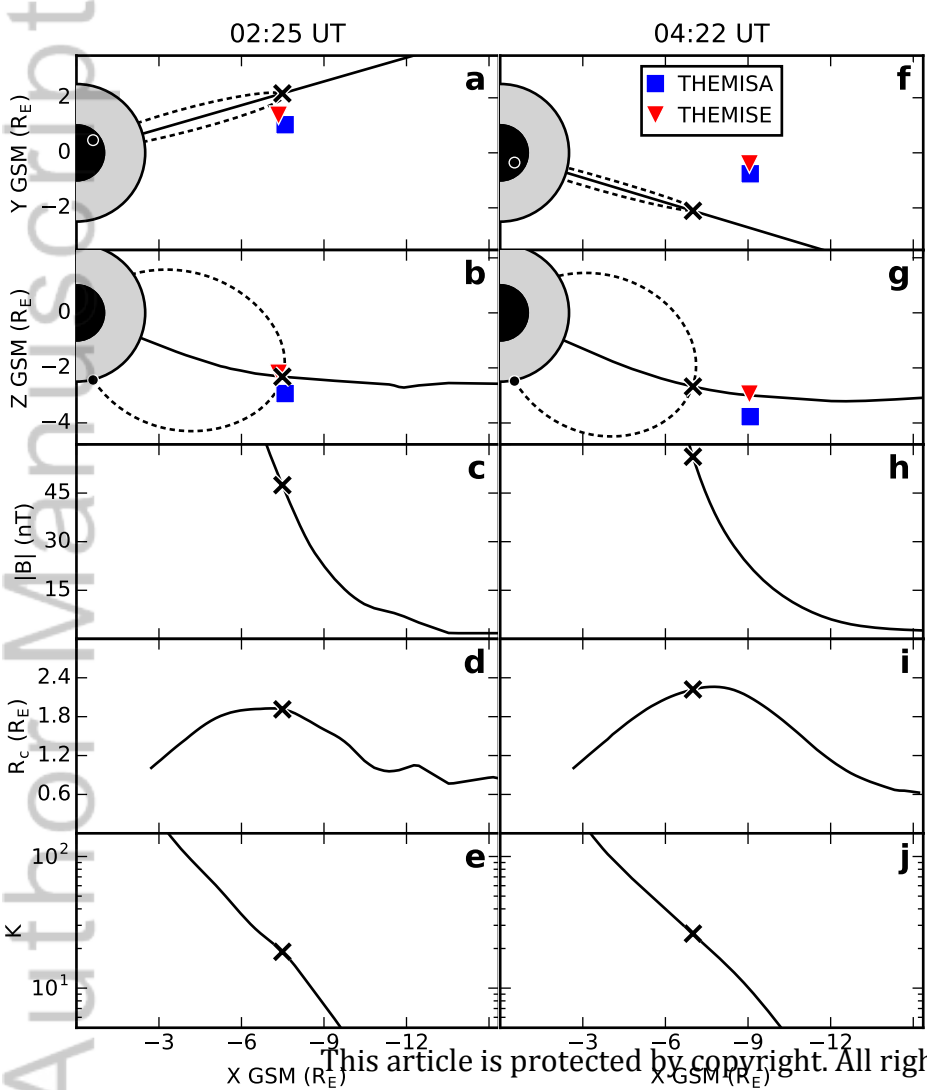

Figure 5.

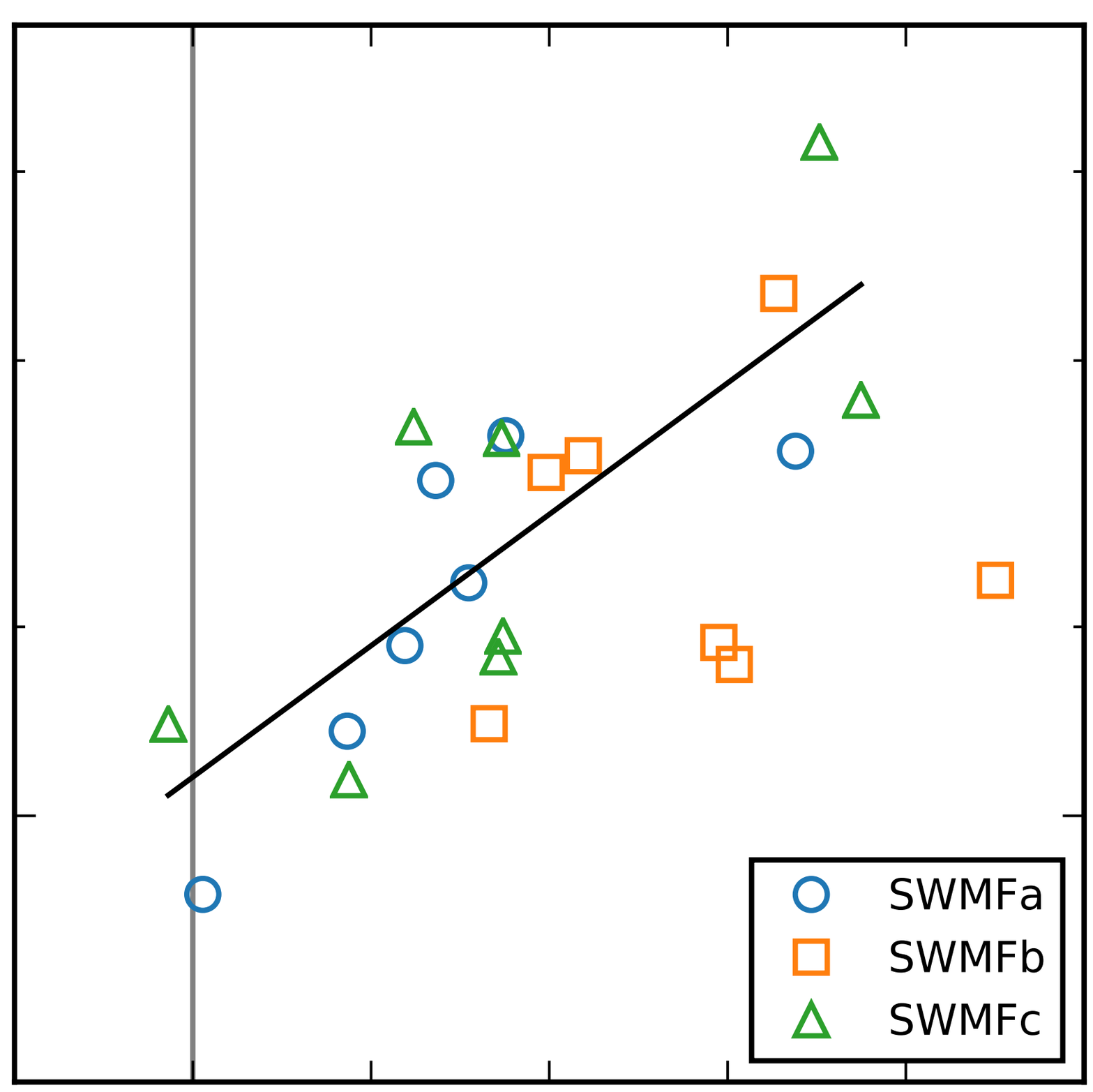

Figure 6.

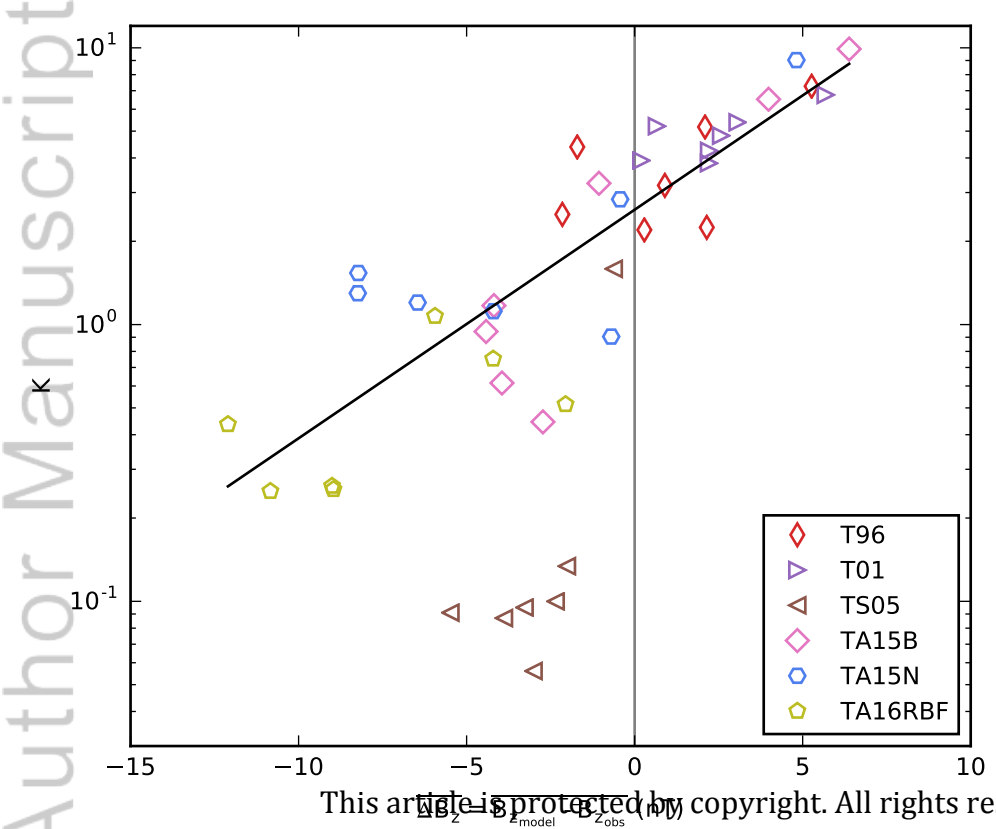

Figure 7.

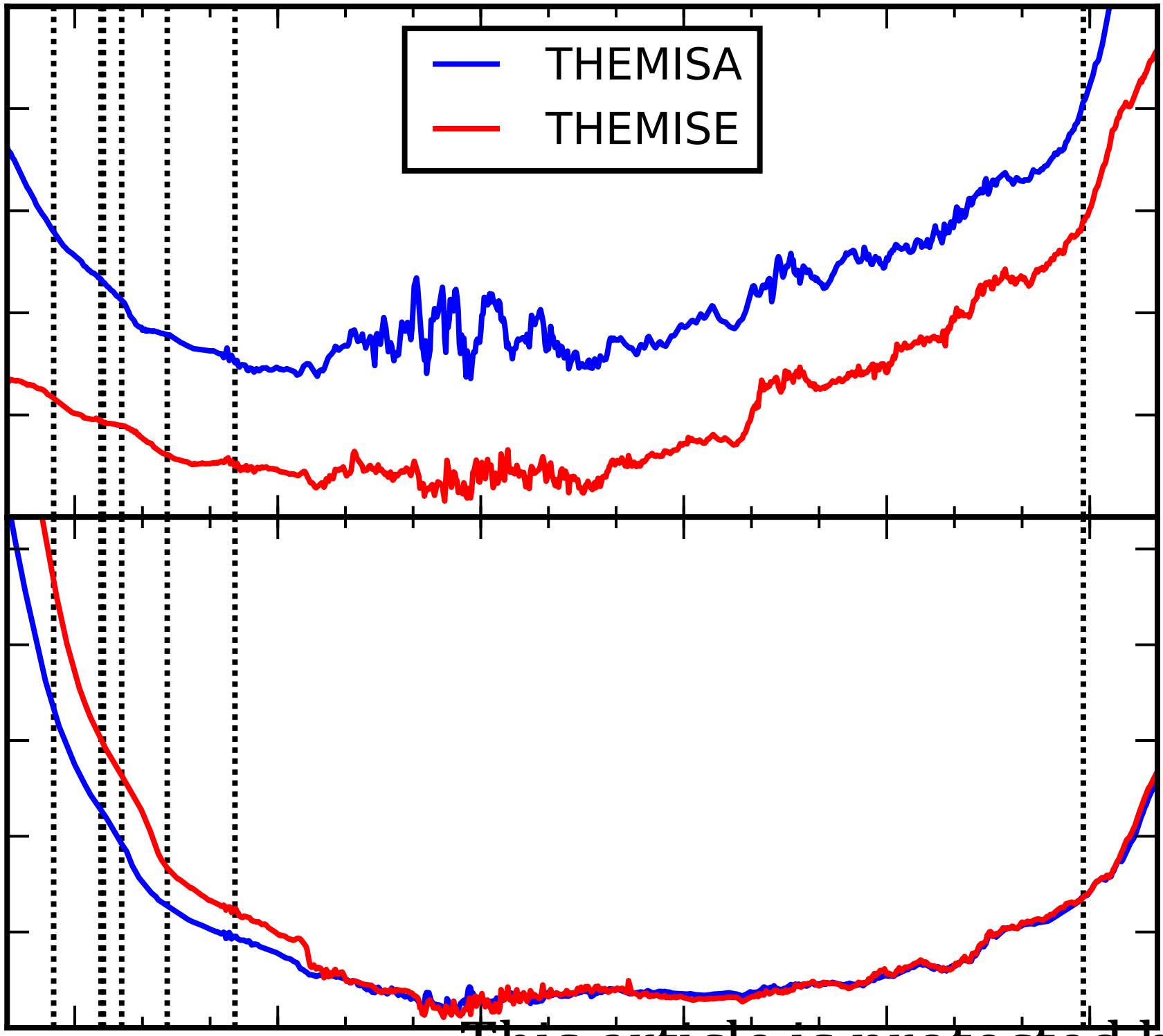

Figure 8.

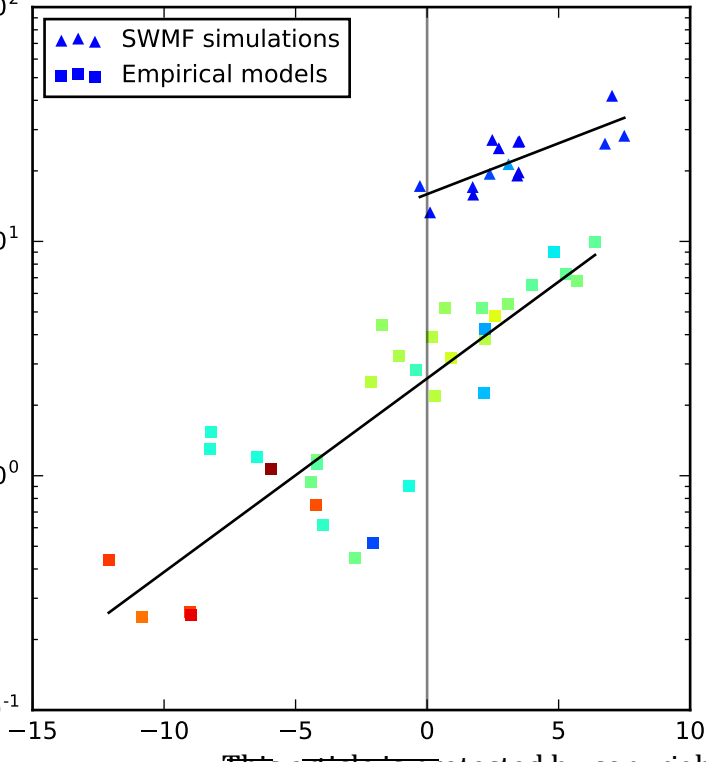

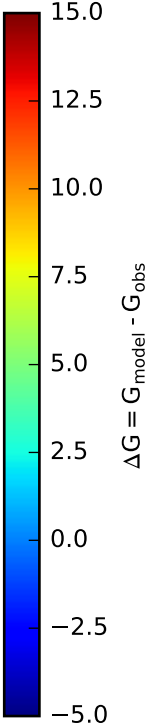

Figure 9.

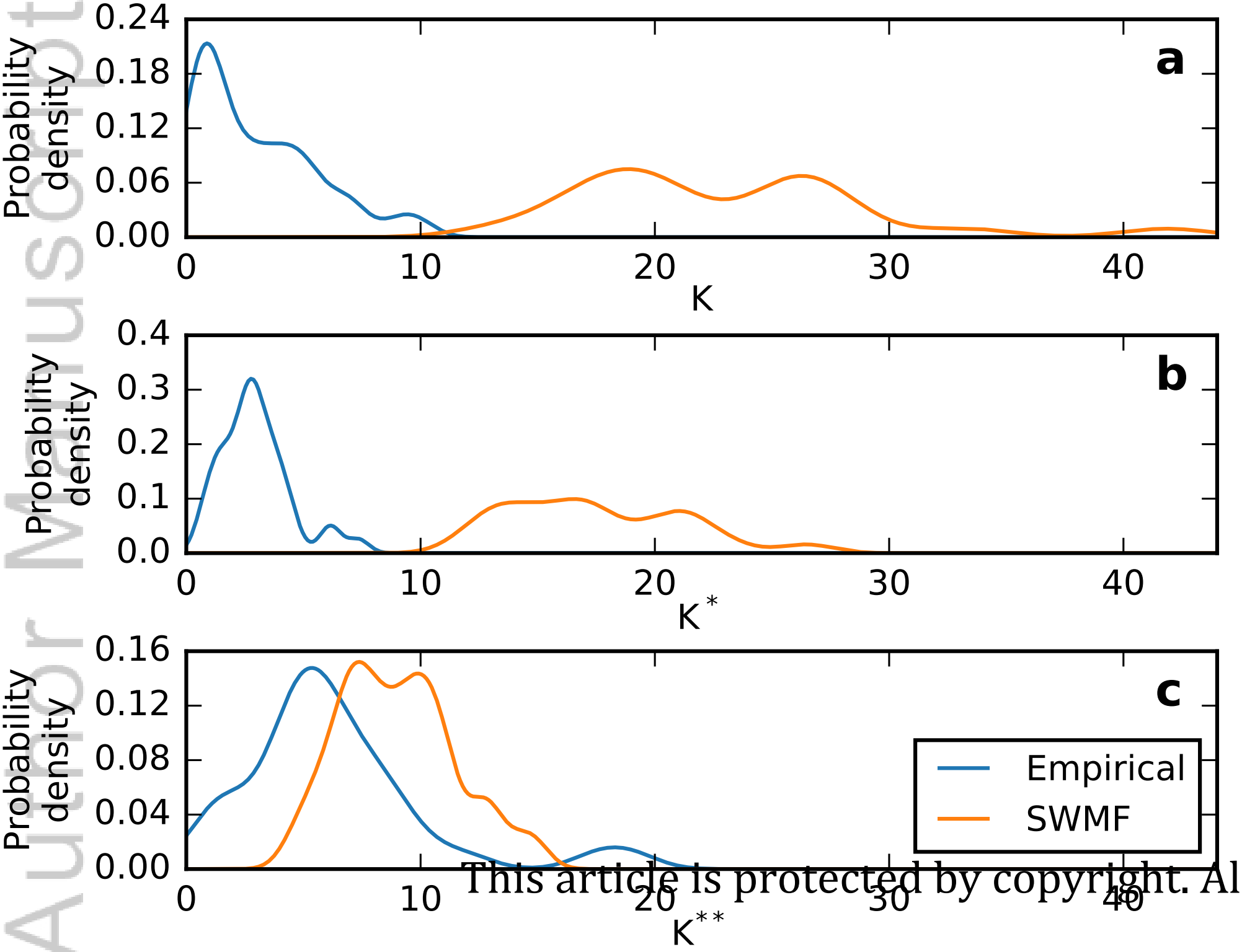

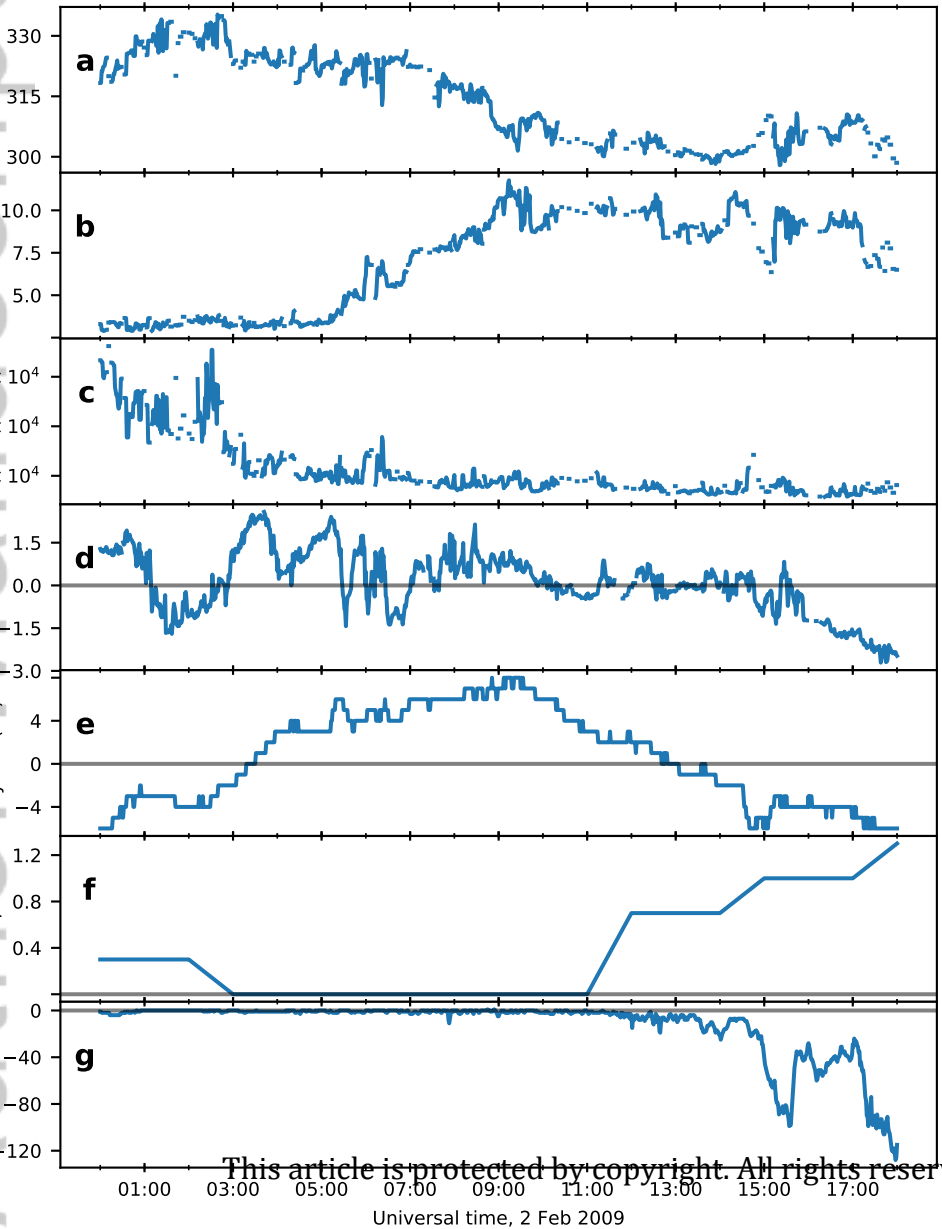

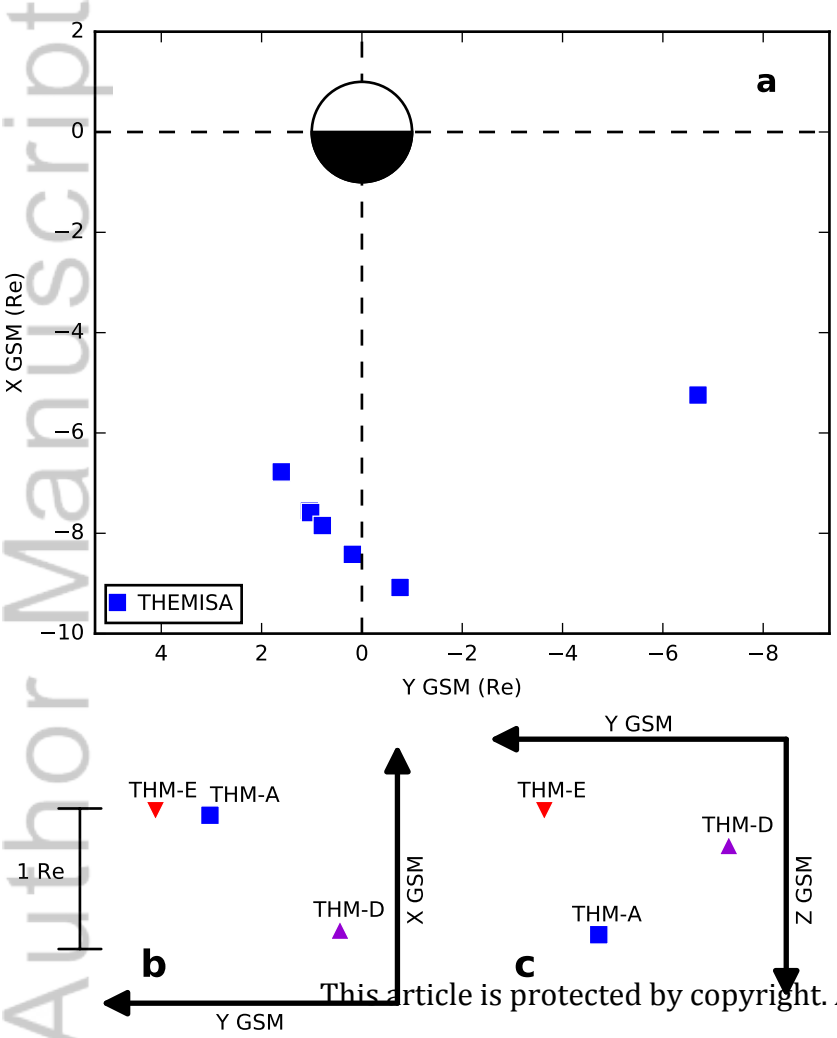

UT	02:00	05:00	08:00	11:00	14:00	17:00	02:00	05:00	08:00	11:00	14:00	17:00
MLT	23.3	0.553	1.48	2.14	2.74	3.49	23.3	0.553	1.48	2.14	2.74	3.49
X GSM	-7.14	-9.4	-10.1	-9.51	-7.89	-5.14	-7.14	-9.4	-10.1	-9.51	-7.89	-5.14
Y GSM	1.37	-1.37	-4.09	-5.98	-6.97	-6.68	1.37	-1.37	-4.09	-5.98	-6.97	-6.68
Z GSM	-2.68	-3.91	-3.81	-3.17	-2.77	-2.49	-2.68	-3.91	-3.81	-3.17	-2.77	-2.49